

AEDC TR-94-7

copy 2

JAN 10 1995

JUN 02 1997

Hypersonic Flight Testing

V. K. Smith

Sverdrup Technology/AEDC Group

and

R. K. Matthews and J. R. Maus

Calspan Corporation/AEDC Operations

August 1994

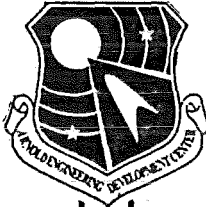
Final Report for Period July 1992 — July 1993

Approved for public release; distribution is unlimited.

**TECHNICAL REPORTS
FILE COPY**

PROPERTY OF U.S. AIR FORCE
AEDC TECHNICAL LIBRARY

**ARNOLD ENGINEERING DEVELOPMENT CENTER
ARNOLD AIR FORCE BASE, TENNESSEE
AIR FORCE MATERIEL COMMAND
UNITED STATES AIR FORCE**



NOTICES

When U. S. Government drawings, specifications, or other data are used for any purpose other than a definitely related Government procurement operation, the Government thereby incurs no responsibility nor any obligation whatsoever, and the fact that the Government may have formulated, furnished, or in any way supplied the said drawings, specifications, or other data, is not to be regarded by implication or otherwise, or in any manner licensing the holder or any other person or corporation, or conveying any rights or permission to manufacture, use, or sell any patented invention that may in any way be related thereto.


Qualified users may obtain copies of this report from the Defense Technical Information Center.

References to named commercial products in this report are not to be considered in any sense as an endorsement of the product by the United States Air Force or the Government.

This report has been reviewed by the Office of Public Affairs (PA) and is releasable to the National Technical Information Service (NTIS). At NTIS, it will be available to the general public, including foreign nations.

APPROVAL STATEMENT

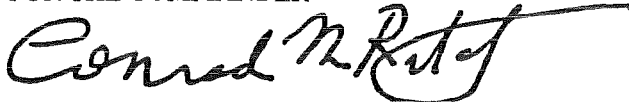
This report has been reviewed and approved:



DENNIS N. HUPRICH, Major, USAF
Space and Missile Systems Test Division

Approved for publication:

FOR THE COMMANDER



CONRAD M. RITCHEY, Lt Col, USAF
Space and Missile Systems Test Division

REPORT DOCUMENTATION PAGE			Form Approved OMB No. 0704-0188	
Public reporting burden for this collection of information is estimated to average 1 hour per response, including the time for reviewing instructions, searching existing data sources, gathering and maintaining the data needed, and completing and reviewing the collection of information. Send comments regarding this burden estimate or any other aspect of this collection of information, including suggestions for reducing this burden, to Washington Headquarters Services, Directorate for Information Operations and Reports, 1215 Jefferson Davis Highway, Suite 1204, Arlington, VA 22202-4302, and to the Office of Management and Budget, Paperwork Reduction Project (0704-0188), Washington, DC 20503.				
1. AGENCY USE ONLY (Leave blank)	2. REPORT DATE August 1994	3. REPORT TYPE AND DATES COVERED Final Report for July 1992 - July 1993		
4. TITLE AND SUBTITLE Hypersonic Flight Testing		5. FUNDING NUMBERS AF Job No. 0979		
6. AUTHOR(S) Smith, V. K., Sverdrup Technology/AEDC Group Matthews, R. K. and Maus, J. R. Calspan Corporation/AEDC Operations				
7. PERFORMING ORGANIZATION NAME(S) AND ADDRESS(ES) Arnold Engineering Development Center/DOF Air Force Materiel Command Arnold Air Force Base, TN 37389-4000		8. PERFORMING ORGANIZATION (REPORT NUMBER) AEDC-TR-94-7		
9. SPONSORING/MONITORING AGENCY NAME(S) AND ADDRESS(ES) Arnold Engineering Development Center/DOF Air Force Materiel Command Arnold Air Force Base, TN 37389-4000		10. SPONSORING/MONITORING AGENCY REPORT NUMBER		
11. SUPPLEMENTARY NOTES Available in Defense Technical Information Center (DTIC).				
12a. DISTRIBUTION/AVAILABILITY STATEMENT Approved for public release; distribution is unlimited.		12b. DISTRIBUTION CODE		
13. ABSTRACT (Maximum 200 words) The challenges of hypersonic system development require a combination of integrated ground testing, flight testing, and computational/simulation approaches. This report addresses the role of flight testing in the triad of development approach and is sub-divided into three parts: - Propulsion, - Aerothermal and - Extrapolation of ground test data to flight. The reasons for propulsion flight test are illustrated by specific mini-case studies. The second part reviews some of the fundamental issues of flight testing and provides an overview of the aerothermal techniques. Specific examples include heat-transfer gage measurements and some of the common problems that have been encountered. The third part of this report discusses the initial flights of the Space Shuttle which uncovered a number of differences between pre-flight aerodynamic predictions and actual flight data. Most notable among these discrepancies was for longitudinal trim during high-speed re-entry. To investigate these differences, several computer codes were applied to a modified Space Shuttle Orbiter to determine aerodynamic parameters over a wide range of conditions. Computations were carried out for wind tunnel conditions and flight conditions to assess Mach number, real gas, and viscous effects on the reentry aerodynamics of the orbiter.				
14. SUBJECT TERMS flight testing, aerothermal techniques, hypersonic vehicles, computational fluid dynamics (CFD) simulations, high-speed re-entry		15. NUMBER OF PAGES 39		
		16. PRICE CODE		
17. SECURITY CLASSIFICATION OF REPORT UNCLASSIFIED	18. SECURITY CLASSIFICATION OF THIS PAGE UNCLASSIFIED	19. SECURITY CLASSIFICATION OF ABSTRACT UNCLASSIFIED	20. LIMITATION OF ABSTRACT SAME AS REPORT	

FOREWORD

The hypersonic regime is the most severe of all flight regimes, and consequently demands smart utilization of ground testing and evaluation, flight testing, and computation/simulation methodologies. Because of this challenge, von Karman Institute (VKI) asked the Arnold Engineering Development Center (AEDC) to develop a comprehensive course to define the "Methodology of Hypersonic Testing." Seven American scientists and engineers, representing AEDC and the University of Tennessee Space Institute (UTSI), formulated this course from their background of over a century of combined experience in hypersonic testing.

The objective of the course was to present a comprehensive overview of the methods used in hypersonic testing and evaluation, and to explain the principles behind those test techniques. Topics covered include an introduction to hypersonic aerodynamics with descriptions of chemical and gas-dynamic phenomena associated with hypersonic flight; categories and application of various hypersonic ground test facilities; characterization of facility flow fields; measurement techniques (both intrusive and non-intrusive); hypersonic propulsion test principles and facilities; computational techniques and their integration into test programs; ground-test-to-flight data correlation methods; and test program planning. The Lecture Series begins at the introductory level and progressively increases in depth, culminating in a focus on special test and evaluation issues in hypersonics such as boundary-layer transition, shock interactions, electromagnetic wave testing, and propulsion integration test techniques.

To obtain a complete set of notes from this course write to:

Lecture Series Secretary
von Karman Institute
Charissie de Waterloo, 72
B-16409 Rhode-Saint-Genese (Belgium)

The information contained in this report is a subset of the work described above.

CONTENTS

	<u>Page</u>
Part I Propulsion Flight Testing	5
Part II Aerothermal Flight Testing	15
Extrapolation of Ground Test Data to Flight.	21

HYPERSONIC FLIGHT TEST PART I PROPULSION FLIGHT TESTING

by
VIRGIL K. SMITH, III
Senior Scientific Principal
Sverdrup Technology, Inc./AEDC Group
Arnold Engineering Development Center

ABSTRACT

The challenges of hypersonic system development require a combination of integrated ground testing, flight testing, and computational/simulation approaches. This lecture addresses the role of flight testing in the triad of development approaches, and focuses specifically on the reasons for hypersonic propulsion flight test. Each reason is illustrated by specific mini-case studies, including the Lockheed X-7, North American X-15/Hypersonic Research Engine (HRE) combination, Russian Hypersonic Flying Laboratory (HFL), National Aeronautics and Space Administration (NASA) SR-71 External Burning Experiment, NASA Space Shuttle, and the German HYTEX Flying Prototype.

NOMENCLATURE

CFD	Computational fluid dynamics
CIAM	Central Institute of Aviation Motors
C.S.	Computation/simulation
CSD	Computational structural dynamics
F.T.	Flight testing
G.T.	Ground testing
HFL	Hypersonic Flying Laboratory
HRE	Hypersonic Research Engine
LOX/LH ₂	Liquid oxygen/liquid hydrogen
NASA	National Aeronautics and Space Administration
NASP	National Aero-Space Plane
SRB	Solid rocket booster
SRM	Solid rocket motor
SSME	Space Shuttle Main Engine
T&E	Test and evaluation

USAF United States Air Force
USN United States Navy

INTRODUCTION

Previous lectures have addressed the use of ground test facilities in the development of hypersonic systems. As discussed in these lectures, while contributing a great deal to hypersonic system development, the current ground test capability has serious and significant limitations. In particular, the severe flight conditions that will be experienced by flight vehicles with air-breathing propulsion systems cannot now be fully simulated in ground test facilities. Full-scale development of these typically slender, lifting, air-breathing hypersonic vehicles will require new facilities. In addition, new test techniques, instrumentation, sensors, and optical access are required.

In addition, the governing physical laws and their consequences in the hypersonic regime are imperfectly understood. This results in important limits of computation and simulation with respect to an understanding of the basic physical phenomena and their appropriate mathematical models. For lack of better information, many computational fluid dynamics (CFD) models use turbulence and real gas models that are empirically based, using qualitative concepts and limited data. A similar situation exists with respect to computational structural dynamics (CSD) models. Although powerful finite-element methods exist, for hypersonic vehicles there is considerable uncertainty about mechanical and thermal loads acting on an overall structure. Also, there are certain structural phenomena that computational models and methods treat only partially, e.g., fatigue, crack propagation, and other failure mechanisms.

Because of these ground test limitations and our lack of total understanding and, hence, modeling and

flight simulation of the hypersonic physics, there are certain key problems that can only be resolved through flight tests. This lecture will focus upon the important contributions of flight testing to hypersonic system development, and will particularly center upon propulsion flight testing. A companion lecture will focus on aerothermal flight testing.

The initial portion of the lecture will consider the many important contributions of flight testing and the three types of hypersonic flight test systems. Next, the traditional and proposed propulsion flight test reasons and traditional/proposed approaches will be reviewed.

Integrated Test and Evaluation

The problems and challenges of hypersonic systems will be properly addressed when ground test data, flight test data, and computational/simulation results are used in combination to support hypersonic research and development (Fig. 1). As shown in Fig. 2, the potential synergism that results from utilization of this triad is especially critical in the development of hypersonic propulsion systems. Whereas in supersonic systems, the state of the art in ground testing, flight testing, and computations/simulations is developed to a roughly balanced state,¹ in contrast, ground test facilities that can simultaneously simulate all of the processes of hypersonic flight over the entire range do not exist. Hence, for hypersonic systems an even larger dependence must be placed upon flight testing and computation/simulation. In addition, the overlap of results from the common areas is essential to provide confidence in the results achieved when overlap is not possible. Uniquely and most importantly, the flight test program provides data to demonstrate that elements of a system function together to perform as designed; in short, it builds confidence! There is currently no other way to assure that the entire system functions as planned.

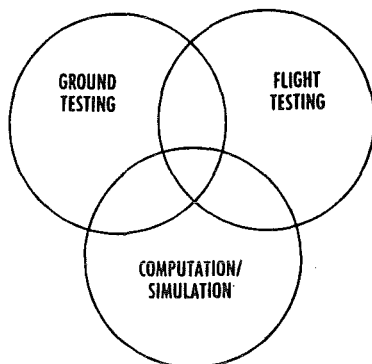


Figure 1. Integrated triad of system development.

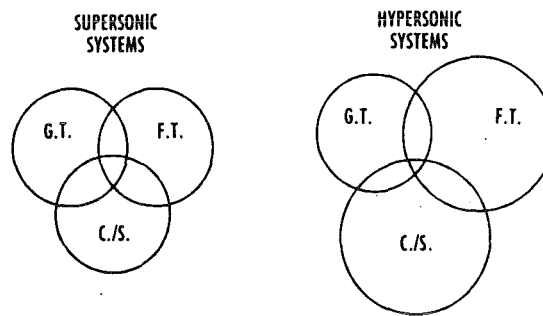


Figure 2. Integrated supersonic and hypersonic development approaches.

Hypersonic Flight Test Systems

As outlined in Ref. 2, a review of hypersonic flight test systems over the last 30 years reveals that three classes of flight test systems are typical, including hypersonic probes, prototype systems, and hybrids. Figure 3 summarizes these system types, their characteristics, and a sampling of historical, recent, and proposed examples. Hypersonic probes, sometimes termed "data probes," are categorized by single-minded flight test objectives which drive the design of the vehicle and its flight operations. Probes are also characterized by short test times commensurate with the acquisition of the narrow data goals defined for the experiment. One reason for this short test time is to eliminate the need for complex thermal protection systems which characterize the hypersonic systems; another reason is to accommodate limited capacity of the system for critical expendables such as fuel.

The X-15/Hypersonic Research Engine (HRE) combination was an excellent example of a hypersonic probe system which extended the X-15 flight test program to focus on propulsion system demonstration. Although the actual HRE never flew on the X-15, the two flights of the X-15 in 1967 with a dummy HRE revealed important airframe-engine interface problems. The intersection of the shock from the engine with the bow shock on the engine strut resulted in the strut burning through and the dummy engine dropping off during landing.³ More details on the historical and current hypersonic probes will be furnished in a later section of this lecture.

Hypersonic prototype systems are categorized by widely diverse flight test objectives which also include the need for measured flight test data (Fig. 3). However, the design of such systems is typically not driven by data, but by other motivations; the data

TYPES AND CHARACTERISTICS	EXAMPLES
PROBES <ul style="list-style-type: none"> • SINGLE-MINDED FLIGHT TEST OBJECTIVES • SHORT TEST TIMES COMMENSURATE WITH DATA GOALS 	AEROTHERMODYNAMICS: <ul style="list-style-type: none"> • REENTRY F EXPERIMENT • VIKING LANDER • FIRE EXPERIMENT
PROTOTYPES <ul style="list-style-type: none"> • WIDELY DIVERSE FLIGHT TEST OBJECTIVES • LONGER TEST TIMES DICTATED BY THE ULTIMATE APPLICATION 	PROPULSION: <ul style="list-style-type: none"> • RUSSIAN HYPERSONIC FLYING LABORATORY (HFL) • LOCKHEED X-7 • X-15/HRE COMBINATION • F-18 EXTERNAL BURNING EXPER. • SR-71 EXTERNAL BURNING EXPER.
HYBRIDS <ul style="list-style-type: none"> • FULLY CAPABLE FLIGHT VEHICLES (FLYING TEST BEDS) • NOT SYSTEM PROTOTYPES 	DYNASOAR (X20-A) APOLLO ROCKWELL SPACE SHUTTLE GERMAN HYTEX JAPANESE HIMES SOIO DC-X X-15 ASSET USAF SVS-D JAPANESE HIMES NASP X-30

Figure 3. Hypersonic flight test systems.³

acquired starts from the premise of the existing flight configuration, rather than shaping it. In addition, the data acquired include both quantitative information as well as more qualitative information (e.g., did the integrated subsystems function as planned?) Hypersonic prototype systems are also characterized by longer test times which are dictated by the ultimate application. These longer test times require the use of complex thermal protection systems and increased capacities for critical system expendables such as fuel. These modifications can complicate some measurements and can lead to multiple and possibly conflicting requirements and objectives from the flight testing operations. The Rockwell Space Shuttle is an excellent example of a manned prototype flight test system having widely diverse flight test objectives with extended test times, culminating in a totally new space transportation system. Key propulsion achievements from the prototype Space Shuttle Orbiter include the demonstration of man-rated, throttleable, liquid oxygen/liquid hydrogen (LOX/LH₂) Space Shuttle main engines (SSMEs) delivering 84,000 N (375,000-lb) thrust from these reusable rocket engines. More details on the historical and current hypersonic prototypes will be furnished in a later section of this lecture.

Hypersonic hybrid systems are categorized by fully capable flight vehicles, sometimes called flying test beds, whose chief function is to provide expansion of the technology database, but the systems are not prototypes of subsequent operational systems. The North American X-15 is an excellent example of hypersonic hybrid systems, as is the planned National Aero-Space Plane (NASP) X-30.

More specific details on these hybrid systems will be furnished in a later section of this lecture.

Flight Test Logistics

The use of flight testing is a major program decision that must be carefully considered. Due to the extremely high cost of flight testing (e.g., typically \$250M minimum),² this method of data acquisition must be weighed against other means. Historically, flight test projects, once initiated, take on an urgency of their own, assuming "...on the day of initiation that the system is behind schedule and never slows down. The timely fabrication of a flight test system becomes more important than the data to be derived from the flight test to the point where compromises are made to the detriment of the test data. This is complicated by the cost factors of such a system which, like the weight of the vehicle, always escalate to the point where the final tasks in the program are neglected as cost-saving items. Data analysis is one of those final tasks. Because of managerial situations such as these, good quality data are difficult to achieve on a flight test program."²

With this general background in propulsion flight testing, subsequent sections will address traditional and future hypersonic flight test rationale and approaches.

PROPULSION FLIGHT TEST APPROACHES

It is instructive for our understanding of the value of propulsion flight test to consider the traditional and current flight test programs, focusing upon the

specific technological achievements and lessons learned. These reasons for flight testing will be examined using a construct offered by numerous authors^{2, 4, 5} and focusing specifically on the reasons for propulsion flight testing.¹ Each reason will be illustrated by specific propulsion flight testing mini-case studies.

- DEMONSTRATE INTERACTIVE TECHNOLOGIES AND IDENTIFY UNANTICIPATED PROBLEMS
- FORM A CATALYST OR FOCUS FOR TECHNOLOGY
- GAIN KNOWLEDGE NOT ONLY FROM THE FLIGHTS BUT ALSO FROM THE PROCESS OF DEVELOPMENT
- DEMONSTRATE TECHNOLOGY IN FLIGHT IN ORDER TO BE CREDIBLE FOR LARGER-SCALE APPLICATIONS
- VALIDATE GROUND TEST DATA AND/OR UNDERSTAND THE BRIDGE BETWEEN GROUND TEST SIMULATIONS AND ACTUAL FLIGHT
- VALIDATE OVERALL SYSTEMS PERFORMANCE
- GENERATE INFORMATION NOT AVAILABLE ON THE GROUND
- PROVIDE AN EFFICIENT EXPANSION OF THE FLIGHT ENVELOPE
- UPDATE THE FLIGHT CONTROL SYSTEM DESIGN AND PROGRAMMING
- UPDATE THE PREDICTED DATABASE EMPLOYED IN THE DEVELOPMENTAL ENGINEERING SIMULATOR

Figure 4. Why flight test?^{2,4,5}

Why Propulsion Flight Testing

In general terms, the reasons for flight testing have been tabulated from several sources by Neumann,² and are repeated in Fig. 4. They range from integrated demonstrations of interactive technologies to specific updating of the predicted database employed in the developmental engineering simulator. In the next several paragraphs, let us understand in more detail these reasons for flight testing as focused upon the propulsion systems.

- **Demonstrate Interactive Technologies** — Although a combination of ground tests and computations/ simulations can be done on individual components or even assemblies of components, flight test is required to demonstrate the interactive technologies and to identify unanticipated problems. In flight, the total flight test system depends not only on how well the individual technologies operate as entities, but also how well they integrate into a flying system. Even the most successful individual technology developments can result in marginal benefits and utility unless they are effectively integrated at the systems level. The demonstration and validation of this synergism are the essence of experimental flight research and the incentive for the investment required.

A good propulsion flight test example for this case was the Rockwell Space Shuttle, which

embodied in the flight test vehicle five individual propulsion engines (Fig. 5). These propulsion systems had been operated individually and collectively in ground test facilities. However, it took the environment of flight test to demonstrate the integrated tripod of propulsion vectors operating in unison during launch, the throttling of the LOX/LH₂ engines to allow safe passage through maximum flight loads, the safe separation of solid rocket boosters, and the throttling to maximum power of the SSMEs to provide orbital insertion.

DESCRIPTION
<p>OBJECTIVES</p> <ul style="list-style-type: none"> • MANNED REUSABLE SPACE TRANSPORTATION SYSTEM <p>CHARACTERISTICS</p> <ul style="list-style-type: none"> • LENGTH: 32 m (122 FT) SPAN: 24 m (78 FT) • EMPTY WEIGHT: 75,000 kg (165,000 LB) • MAN-RATED THROTTLEABLE LOX/LH₂ SSMEs <ul style="list-style-type: none"> — 84,300 N (375,000 LB) Thrust — Reusable • SEGMENTED SOLID ROCKET BOOSTERS (SRBs) <p>PERFORMANCE</p> <ul style="list-style-type: none"> • MANNED ORBITAL SPACE FLIGHT • PAYLOAD DEPLOYMENT AND RETRIEVAL <p>APPROACH</p> <ul style="list-style-type: none"> • USE TRIPOD OF PROPULSION ENGINES TO POWER LIFTOFF • SEPARATE SRBs FOLLOWING EXPENDITURE • UTILIZE THROTTLEABLE SSMEs TO PROVIDE ORBITAL INSERTION <p>TECHNOLOGICAL ACHIEVEMENTS</p> <ul style="list-style-type: none"> • FULL FLIGHT ENVELOPE VALIDATION FOR LAUNCH, SPACE, AND REENTRY OPERATIONS • THROTTLEABLE, REUSABLE LIQUID ROCKET ENGINES • SEPARATION OF EXPENDABLE SOLID ROCKET MOTORS (SRMs) <p>LESSONS LEARNED</p> <ul style="list-style-type: none"> • ENVIRONMENTAL EXTREMES EFFECTS ON SUBCOMPONENTS

Figure 5. Space shuttle flight test example.³

The X-15/HRE combination, a supplementary flight test program accomplished after the original 3 year flight test program, provided an excellent example of flight testing identifying unanticipated problems (Fig. 6). The dummy ramjet experiment carried at high flight velocities resulted in almost catastrophic effects resulting from shock boundary-layer interaction and the significantly increased interference heating that was generated. From this unanticipated information came increased research and development which influenced the design of subsequent vehicles.⁴

- **Form a Catalyst or Focus for Technology** — A flight test program can serve as a focusing effort for the technologies in the hypersonic regime, and the findings and lessons learned

DESCRIPTION	
OBJECTIVES	<ul style="list-style-type: none"> • DEMONSTRATE RAMJET/SCRAMJET PROPULSION OPERATION IN SUPERSONIC AND HYPERSONIC ATMOSPHERIC FLIGHT • HYDROGEN FUELED
CHARACTERISTICS	<ul style="list-style-type: none"> • ENGINE LENGTH: 218-231 cm (86-91 IN.) • INLET DIAMETER: 46 cm (18 IN.) • NOZZLE DIAMETER: 63.75 cm (25.1 IN.)
PERFORMANCE	<ul style="list-style-type: none"> • MACH 6.7 • ALTITUDE: 100 km (328,000 FT)
APPROACH	
	<ul style="list-style-type: none"> • USE X-15 AS PROPULSION FLYING TESTBED • PERFORM TWO INTEGRATION FLIGHTS WITH DUMMY ENGINE • PERFORM FLIGHT TEST WITH GARRETT HYPERSONIC RESEARCH ENGINE (HRE)
TECHNOLOGICAL ACHIEVEMENTS	
	<ul style="list-style-type: none"> • TWO FLIGHTS IN 1967 WITH DUMMY ENGINE <ul style="list-style-type: none"> — Revealed Shock Interactions and Deleterious Effects of Heating Gradients, Geometry Effects, and Local Heating
LESSONS LEARNED	
	<ul style="list-style-type: none"> • CANCELLATION OF X-15 PROGRAM IN JANUARY 1968 RESULTED IN HRE GROUND TEST ONLY • ENGINE-AIRFRAME INTEGRATION SURPRISE

Figure 6. X-15/HRE flight test example.^{3,6}

can serve as a catalyst for technology developments. The planned NASP X-30 flight test program is the latest example of this focused technology. The accelerated development and application of CFD for vehicle and propulsion design serve as a good example case.³ The increasing cost effectiveness of and advances in computers, CFD methods, and display graphics have in large part been energized by the desire to model complex NASP internal and external hypersonic geometries with the proper physics. This has allowed CFD to be propelled from a novelty, or at best a check against a wind tunnel-developed design, to a viable design tool with the wind tunnel used as confirmation of the selected design. The increasingly high confidence in predictions being produced by CFD will also provide data which are not available from ground test facilities to allow a commitment to flight research for full design validation.

There are many more examples of this process. Further back in history, the Space Shuttle dominated thinking and technology development of hypersonic vehicles. Prior to the Shuttle, the X-15 dominated. The X-15 not only provided a focus for hypersonics research, but also provided a stimulus for basic

research in this area. As of mid-1968, the technical community wrote 766 reports addressing X-15 development, flight test, and general research inspired by the X-15 program.⁴ Hence, knowledge was gained, not only from the flights, but also from the process of development.

DESCRIPTION	
OBJECTIVES	<ul style="list-style-type: none"> • SUPERSONIC/HYPERSONIC RAMJET ENGINE TESTBED
CHARACTERISTICS	<ul style="list-style-type: none"> • LENGTH: 10 m (33 FT) • SPAN: 3.7 m (12 FT) • GROSS WEIGHT: 3640 kg (8,000 LB)
PERFORMANCE	<ul style="list-style-type: none"> • MACH 4.3 • ALTITUDE: 30,480+ m (100,000+ FT) • RANGE: 158+ km (100+ MILES)
APPROACH	
	<ul style="list-style-type: none"> • UTILIZE A VERSATILE, FULL-SCALE TESTBED FOR SUPERSONIC AND HYPERSONIC RAMJET PROPULSION • ROCKET BOOST VEHICLE TO VELOCITIES SUITABLE FOR RAMJET-POWERED FLIGHT OVER A WIDE RANGE OF MACH NUMBERS AND ALTITUDES • AIR/GROUND LAUNCHED, ROCKET BOOSTED, PARACHUTE RECOVERY
TECHNOLOGICAL ACHIEVEMENTS	
	<ul style="list-style-type: none"> • SUSTAINED RAMJET TESTING UP TO MACH 4.3 • DATABASE PROVIDED VALIDATION FOR MANY RAMJET CONFIGURATIONS AND THE BOMARC SYSTEM <ul style="list-style-type: none"> — Aero: Extensive High Mach Propulsion Performance and Control Data; Airframe Instrumentation — Thermo: Mach 4+ Environment — Propulsion: Ramjet Database for Bomarc; Tested XRJ47, XRJ43, and XRJ59 Engines; Boron Fuel Experiments — Subsystems: In-flight Drag Modulation, Preprogrammed Flight Profile
LESSONS LEARNED	
	<ul style="list-style-type: none"> • IN PERIOD 1947-1960, PROVIDED MEANS OF ADVANCING TECHNOLOGY AND VALIDATING DATABASE FOR NEW MISSILE PROPULSION SYSTEM • FIRST MACH 3+ FULL-SCALE REUSABLE RESEARCH AIRCRAFT

Figure 7. Lockheed/USAF/USN X-7 hypersonic propulsion flight test prototype.^{3,6}

- Demonstrate Technology in Flight in Order to be Credible for Larger-Scaled Applications — In order to integrate new flight vehicle technology into commercial or military systems, demonstration of that technology beyond the component stage and through flight testing is required. A classic propulsion example of this approach was the Lockheed X-7 program.^{3,6} The X-7 program, conducted between 1947 and 1960, proved to be an extremely versatile full-scale testbed for supersonic and hypersonic ramjet propulsion (Fig. 7). This system was capable of ground- or air-launched research flights, and it was rocket boosted to velocities suitable for ramjet-powered flight over a wide

range of Mach numbers and altitudes. During the extensive flight test program, sustained ramjet testing was performed up to Mach 4.3, a performance high point for this unmanned, reusable system. The generated database was critical to validation of many ramjet configurations, and was the basis for the Bomarc ground-to-air missile propulsion system.

Comparable utilization of flight test demonstration of advanced ramjet propulsion technology was accomplished in France on the ONERA Mach 5 STALTEX experimental missile.⁷ The proposed HYTEX flight demonstrator for subscale demonstration of SAENGER propulsion and propulsion integration,^{8, 9, 10} is also an example of demonstrating propulsion technology in flight prior to larger-scale applications. This specific example will be addressed in more detail later in this lecture.

- Validate Ground Test and Evaluation Data and/or Understand the Bridge Between Ground Test Simulations and Actual Flight — Validation of ground test data and/or the validation of processes that transform that ground test data to flight applications is always a need in flight test, and frequently it is not achieved. Classical examples of this have been reported.^{11, 12} Typical propulsion examples include the Russian Hypersonic Flying Laboratory (HFL), which will be discussed later in this lecture, the F/A-18 External Burning Flight Test,¹³ and the proposed National Aeronautics

and Space Administration (NASA) Dryden SR-71A External Burning Flight Test.¹⁴

The details of the latter flight test application are summarized in Fig. 8. This captive-carry flight test experiment utilizes the transonic external burning concept with gaseous hydrogen fuel to provide the first large-scale flight test investigation of this base drag reduction technique at Mach numbers up to 3. Low-speed base drag reduction is important in reducing vehicle drag and improving propulsive nozzle efficiency, and there have even been claims of positive thrust generation. Flight data will be correlated with a concurrent wind tunnel ground test of a similar test apparatus to confirm geometry and component performance scalability predictions and to investigate design parametrics under actual flight conditions.

- Validate Overall Systems Performance — Answering the question “Did the vehicle perform as anticipated?” is one of the most important reasons to conduct flight test. The collection of interactive technologies, the demonstration of their interactions, and the assessment of systems through an efficient expansion of the flight envelope are key requirements in certifying a collection of hypersonic technology as ready for transfer to operational vehicles.

Typical propulsion examples include the NASP X-30,^{15, 16, 17} the Space Shuttle,^{2, 3} and the proposed

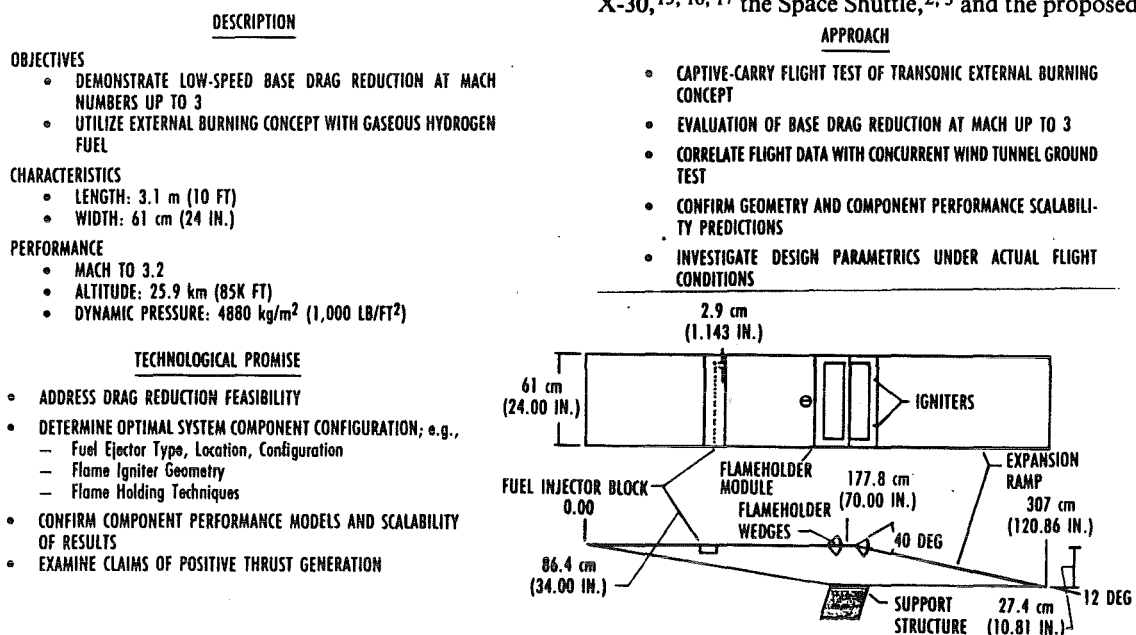
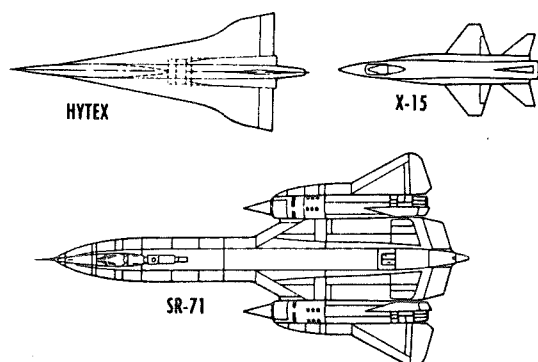


Figure 8. SR-71A external burning flight test.¹⁴

- DESCRIPTION
- OBJECTIVES**
- DEMONSTRATE SAENGER TURBO-RAM PROPULSION SYSTEM IN SUPERSONIC AND HYPERSONIC ATMOSPHERIC FLIGHT
 - KEROSENE/HYDROGEN FUEL
- CHARACTERISTICS**
- LENGTH: 23 m (75.44 FT)
 - WINGSPAN: 9.3 m (30.5 FT)
- PERFORMANCE**
- MACH 5.5
 - ALTITUDE: 30 km (98,430 FT)
- APPROACH
- DESIGN, FABRICATION, AND FLIGHT TEST OF A SUBSCALE RESEARCH VEHICLE REPRESENTATIVE OF SAENGER CONCEPT
 - EVALUATE PROPULSION PERFORMANCE OVER THE FLIGHT ENVELOPE OF THE SAENGER FIRST STAGE
 - COLLECT DEVELOPMENT AND FLIGHT TEST DATA FOR CODE AND DESIGN VALIDATION
- TECHNOLOGICAL PROMISE
- DEMONSTRATE PROOF OF FEASIBILITY OF SAENGER PROPULSION SYSTEM
 - Inlet
 - Turbojet and Ramjet Engine
 - Nozzle
 - Mode Transition and Control
 - Airframe/Engine Integration
 - VERIFICATION OF AEROTHERMODYNAMIC COMPUTATIONAL METHODS AND CODES, STRUCTURAL DESIGN, AND SUBSYSTEMS, ESPECIALLY FLIGHT CONTROL



	X-15	SR-71	HYTEX
MAX. SPEED (M)	6,5	3,5	5,5
MAX. ALTITUDE	100 KM (328 KFT)	25 KM (82 KFT)	30 KM (98 KFT)
PROPULSION SYSTEM	ROCKET	TURBO	TURBO-RAM
MODEL OF LAUNCH	AIR	GROUND	GROUND

Figure 9. German HYTEX flight test prototype.^{9,10,18}

German HYTEX flight demonstrator for the SAENGER aerospace plane system.^{9, 10,18}

The details of the HYTEX propulsion flight demonstrator are shown in Fig. 9. This proposed program provides a demonstration of the proof of feasibility of an integrated SAENGER propulsion system through design, fabrication, and flight test of

a subscale research vehicle representative of the SAENGER concept. The flight test program will evaluate integrated turbo-ramjet propulsion system performance over an expansion of the flight envelope to Mach 5.5 at 30 km, and in the process collect data for validation of aerodynamic and propulsion codes. Reference 10 indicated that this HYTEX concept was being broadened to consider a family of hypersonic experimental flight vehicle alternatives, ranging from unmanned test vehicles to manned hypersonic test aircraft. It was noted that both technical and financial feasibility must be proven before a selection can be made.

- Update the Predicted Database Employed in the Developmental Engineering Simulator — A variety of computational models and flight simulators are typically utilized to support flight systems technology development and flight test planning. A typical example of computational models are trajectory models which are utilized to optimize the ascent and descent flight paths. These models utilize a mathematical description of the flight vehicle which contains numerous assumptions about the vehicle characteristics. Hypersonic simulation models which describe processes such as atmospheric variability, aerodynamic heating, and propulsion system operating dynamics are typically developed for incorporation into high-fidelity, real-time, man-in-the-loop simulations. These simulations are then used to evaluate flying quality criteria over the hypersonic flight regime. The simulators are then utilized to gain thorough understanding of required versus potential vehicle flying qualities, which are utilized for the integrated flight control system. The engineering models and simulations are based upon experience from past vehicles and "best guess," and flight testing is utilized to collect data for updating of the various developmental engineering simulations.

A typical example of using flight test to update the propulsion engineering simulations is provided by the Russian HFL. It is reported that the typical Russian approach to propulsion system development is the utilization of engine mathematical models to predict and optimize cycle performance.^{19, 20} Recent flight testing of the Central Institute of Aviation Motors (CIAM)/Soyuz Design Bureau Hypersonic Flying Laboratory (HFL) has had as one major objective the validation of ground simulations.^{20, 21, 22} Using ground test data, the Russians have

DESCRIPTIONOBJECTIVES

- DEMONSTRATE RAMJET/SCRAMJET PROPULSION OPERATION IN SUPERSONIC AND HYPERSONIC ATMOSPHERIC FLIGHT
- LIQUID HYDROGEN FUELED

CHARACTERISTICS

- LENGTH: 4.3 M ENGINE LENGTH: 1.28 M
- DIAMETER: 0.75 M ENGINE DIAM.: 0.23 M
- WEIGHT: 595 KG FUEL: 17 KG

PERFORMANCE

- MACH 6-8
- ALTITUDE: 30 km (98K FT)

APPROACH

- USE GROUND-TO-AIR MISSILE AS PROPULSION FLYING TESTBED
- EVALUATE SUBSCALE AXISYMMETRIC RAMJET/SCRAMJET MOUNTED WITH UTILITIES ON MISSILE NOSE
- PERFORM INTEGRATION FLIGHTS WITH COLD ENGINE FLOW
- PERFORM HOT FLOW ENGINE TEST FLIGHTS
- EXPAND ENGINE PERFORMANCE ENVELOPE

TECHNOLOGICAL ACHIEVEMENTS

- TWO INTEGRATION FLIGHTS WITH COLD ENGINE FLOW (1989, 1990); TRAJECTORY VERIFICATION
- TWO HOT FLOW ENGINE TEST FLIGHTS
 - Nov. 1991: Mach 5.8 at 25 km Reported 30 Sec of Engine Operation; Ramjet to Scramjet Transition; 5 Sec of Scramjet Operation; Engine Recovered
 - Nov. 1992: Reported 17 Sec of Engine Operation; Ramjet to Scramjet Transition; 15 Sec of Scramjet Operation

LESSONS LEARNED

- DEMONSTRATED STAGED INJECTION OF FUEL TO CONTROL SUBSONIC AND SUPERSONIC COMBUSTION
- DEMONSTRATED REGENERATIVE COOLING OF COMBUSTOR WALL WITH LIQUID HYDROGEN
- VERIFIED ALTITUDE REIGNITION OF THE ENGINE
- DIFFICULTY OF EXPANDING THE AXISYMMETRIC ENGINE RESULTS TO A REALISTIC ENGINE CONFIGURATION

Figure 10. Russian Hypersonic Flying Laboratory.^{20, 21, 22}

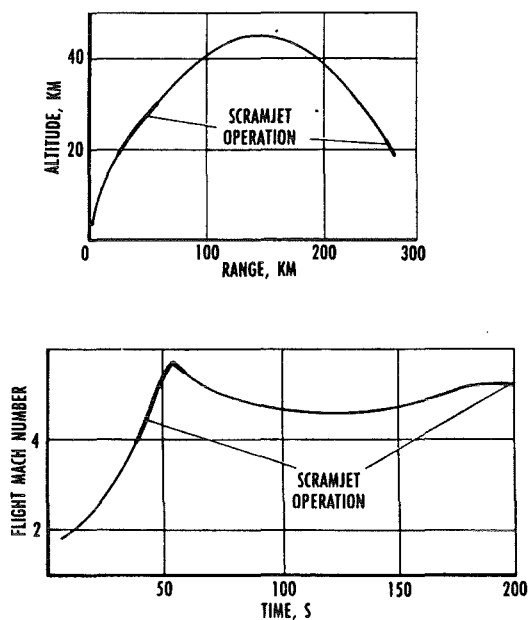


Figure 11. HFL flight test data.¹²

accomplished one-dimensional calculations that approximate the ramjet/scramjet combustion process. Flight test data will help verify the accuracy of those codes. The HFL description, program objectives, and achievements are addressed in Fig. 10. This flight test program of a subscale, axisymmetric ramjet/scramjet missile mounted with controls and expendables atop a Russian ground-to-air missile demonstrated a number of achievements in its four test flights. Most importantly, it demonstrated staged injection of hydrogen fuel into the combustion chamber in order to control subsonic and supersonic combustion. It also utilized liquid hydrogen fuel to provide regenerative cooling to the combustor wall, injecting gaseous hydrogen through one of three rows of injectors; injector rows were alternated depending upon flight conditions to change the engine's mode of combustion. The flights also revealed the need to explore a different ramjet/scramjet configuration in order to approach a real engine configuration. Typical engine flight test data are shown in Fig. 11. These flight test data are useful both for validating the ground test data and for updating the predicted database involved in the engineering modes and simulations.

CONCLUSION

Without a doubt, propulsion flight testing of hypersonic vehicles offers a challenge comparable to testing the Lockheed X-7 and the North American X-15. Concepts range from unmanned test vehicles to manned hypersonic test aircraft (Fig. 12). For these research vehicles and programs, trades clearly must

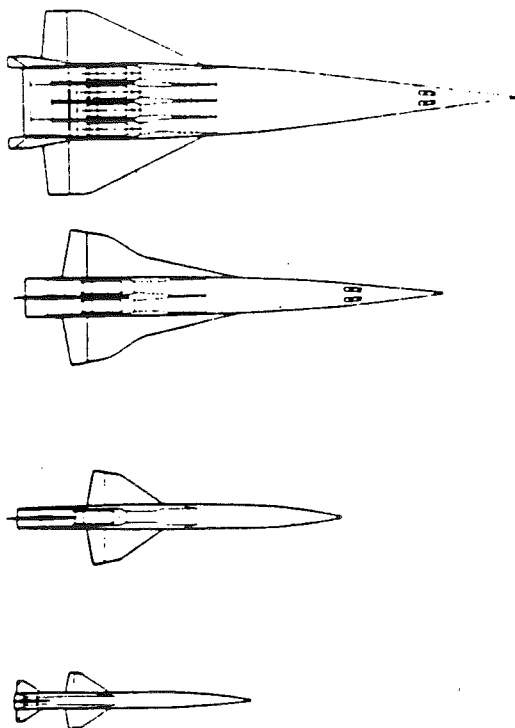


Figure 12. Hypersonic experimental vehicle alternatives.¹⁸

be made between the ground tests, flight tests, and computations/simulations and the impact of these methodologies on the vehicle design. Both the technical as well as the financial feasibility must be examined in order to assemble a test and evaluation (T&E) approach which maximizes returns. Many aspects have to be considered, and realistic integrated, cooperative scenarios have to be established. This lecture has addressed the important aspects to be considered in propulsion flight testing.

REFERENCES

1. Smith, V. K. "The Complementary Role of Ground Testing and Flight Testing in Engine Development." AIAA-87-1850, AIAA Joint Propulsion Conference, San Diego, Calif., 1987.
2. Neumann, R. D. "Flight Test Validation." Short Course on Scramjet Technology, University of Tennessee Space Institute, March 30-April 3, 1987.
3. Gulcher, R. H. "The Past as Prologue." AIAA-89-5004, AIAA First National Aerospace Plane Conference, Dayton, Ohio, July 20-21, 1989.
4. Draper, A. C., Buck, M. L., and Selegan, D. R. "Aerospace Technology Demonstrators/Research and Operational Options." AIAA-83-1054, AIAA Aircraft Prototype and Technology Demonstrator Symposium, 1983.
5. Kirsten, P. W. and Richardson, D. F. "Predicted and Flight Test Results of the Performance and Stability and Control of the Space Shuttle from Reentry to Landing." AGARD Report CP-339, 1982.
6. Miller, J. *The X-Planes: X-1 to X-31*. Orion Books, 1988.
7. Marguet, R., Berton, P., and Hirsinger, F. "L'Etude du Statoreacteur Supersonique et Hypersonique en France de 1950 a' 1974." AGARD Conference Proceedings No. 479, Hypersonic Combined Cycle Propulsion, Madrid, Spain, 28 May-1 June 1990.
8. Lederer, R. and Schwab, R. "Hypersonic Airbreathing Propulsion Activities for SAENGER." AIAA-91-5040, AIAA Third International Aerospace Planes Conference, Orlando, Florida, 3-5 December 1991.
9. Kuczera, H. and Sacher, P. "The German Hypersonics Programme-Status Report." AIAA-91-5001, AIAA Third International Aerospace Planes Conference, Orlando, Florida, 3-5 December 1991.
10. Kuczera, H. and Hauck, H. "The German Hypersonics Technology Programme-Status Report 1992." Paper IAF 92-0867, 43rd Congress of the International Astronautical Federation, Washington, DC, 1992.
11. Lukasiewicz, J. *Experimental Methods in Hypersonics*. Marcel Dekker, Inc., 1973.
12. Griffith, B. J., Maus, J. R., Majors, B. M., and Best, J. T. "Addressing the Hypersonic Simulation Problem." AIAA-86-9775, 1986.
13. Yungkurth, C., C'orda, S., Dawson, F., and Houck, S. "The F/A-18 External Burning Flight Test." AIAA-91-5050, Third International Aerospace Planes Conference, December 1991.

14. Hicks, J. W. "Development of a Hydrogen External Burning Flight Test Experiment on the NASA Dryden SR-71A Aircraft." SAE 920997, 1992 SAE Aerospace Atlantic Conference, Dayton, Ohio, April 7-10, 1992.
15. Wierzbanski, T. "The Challenge of X-30 Flight Test." AIAA-89-5015, AIAA First National Aero-Space Plane Conference, Dayton, Ohio, July 20-21, 1989.
16. Parks, S., and Waldman, B. "Flight Testing Hypersonic Vehicles—The X-30 and Beyond." AIAA-90-5229, AIAA Second International Aerospace Planes Conference, Orlando, Florida, October 29-31, 1990.
17. Brown, K. G., Erbland, P., Gilbert, W., and Hicks, J. "National Aero-Space Plane Research Program Plan." AIAA Fourth International Aerospace Planes Conference, Orlando, Florida, December 1-4, 1992.
18. "Hypersonic Experimental Aircraft Technology Demonstrator HYTEX." MBB Report 797-390, December 1991.
19. Sosounov, V. A. "Study of Propulsion for High Velocity Flight." 10th Symposium of International Society of Air Breathing Engines, Nottingham, U.K., September 1991.
20. Krjutschenko, V. V. and Rudakov, A. S. "Effect of Scramjet Components Operating Process Effectiveness of Engine Configuration." SAE 920995, 1992 SAE Aerospace Atlantic Conference, Dayton, Ohio, April 7-10, 1992.
21. Kandebo, S. W. "Russians Want U.S. to Join Scramjet Tests." *Aviation Week & Space Technology*, March 30, 1992.
22. Kandebo, S. W. "Franco-Russian Tests May Spur New Projects." *Aviation Week & Space Technology*, December 14/21, 1992.

HYPERSONIC FLIGHT TESTING PART II AEROTHERMAL FLIGHT TESTING

by
R. K. MATTHEWS
Senior Staff Engineer
Calspan Corporation/AEDC Operations
Arnold Engineering Development Center

ABSTRACT

Flight testing is an integral part of the hypersonics testing methodology. It provides the only true environment to demonstrate that the vehicle has the material/structural integrity to survive hypersonic flight. This section reviews some of the fundamental issues of flight testing and provides an overview of the aerothermal techniques. Specific examples include heat-transfer gage measurements and some of the common problems that have been encountered.

NOMENCLATURE

h	Heat-transfer coefficient
h_{STAG}	Stagnation point heat-transfer coefficient
k	Material conductivity
L	Body length
M_{∞}	Free-stream Mach number
\dot{q} , QDOT	Heating rate (1 Btu/ft ² -sec $\approx 1\text{w/cm}^2$)
R	Radial distance from centerline
R_N	Nose radius
R_{∞}	Free-stream Reynolds number
T_r	Recovery temperature
T_w	Wall temperature
ΔT	Temperature difference
X	Axial distance from nose
c	Material specific heat
ϵ	Emmissivity
ρ	Material density

FUNDAMENTALS

The development of hypersonic vehicles is based on a foundation of three disciplines:

Ground Testing
Analysis (CFD) and
Flight Testing*

It is extremely important that each of these areas provide high-quality information and that there is an interactive flow of this information. Unfortunately, there are sometimes "simplistic overviews" that confuse the issues as illustrated in Fig. 1. Flight testing is very expensive, and historically there have been several programs cancelled immediately following a flight test failure. On the other hand there is "Reality" as shown in Fig. 2. CFD simulations are often "adjusted" to match experiments and in general they need to be coupled with experiments. Wind tunnels also have real-world problems in terms of simulation issues and extrapolation of the data to flight. The important message is that flight testing is needed (Fig. 2c) to demonstrate that the vehicle has material/structural integrity in the true environment and that the hardware and software can function properly in the environment so that the vehicle performs the required mission.

One of the key aspects that a flight test program should include is a large effort to predict the results in terms of aerodynamics, vehicle dynamics, aerothermodynamics, and material behavior (Fig. 3).

* One of the leading organizations involved in hypersonic flight testing in the U.S. is the Sandia National Laboratories (SNL) and much of the information in these notes was obtained from them (see Ref. 1).

CFD IS WONDERFUL
 WIND TUNNELS ARE WONDERFUL
 FLIGHT TESTING IS
 EXPENSIVE
 REQUIRES LONG PREPARATION TIME
 PRONE TO PRODUCE FAILURES
 RESULTS MAY KILL PROGRAM

Figure 1. Simplistic overview.

IN GENERAL, OBSERVATIONS LEAD TO THEORY
 CFD MODELS ARE ADJUSTED TO MATCH EXPERIMENTS
 CFD DOES NOT ACCURATELY PREDICT ALL FUTURE TESTS
 COUPLED WITH WIND TUNNEL TEST IT IS USED TO STUDY
 — INTERMEDIATE MACH AND REYNOLDS NUMBER
 — SMALL VEHICLE GEOMETRY CHANGES

a. Simulation (CFD)

REYNOLDS NUMBER IS OFTEN WRONG
 MACH NUMBER MAY BE WRONG
 TUNNEL CONDITIONS BAD
 FLOW ANGULARITY AND NONUNIFORMITIES
 BASE FLOW ISSUES
 MODELS ARE TOO SMALL
 TUNNELS ARE THE MOST EFFICIENT WAY TO ACCURATELY STUDY
 ANGLE OF ATTACK
 ROLL ANGLE
 SURFACE DEFLECTION
 VEHICLE GEOMETRY

b. Wind tunnel test

IT PROVIDES THE TRUE ENVIRONMENT (NO SIMULATION) WHICH ALSO INCLUDES
 CONTINUOUS CHANGES IN ENVIRONMENT
 IT IS THE ONLY WAY TO SHOW THE HARDWARE AND SOFTWARE PERFORMS ITS MISSION

c. Flight test

Figure 2. Reality.

LARGE EFFORT PREFLIGHT IN PREDICTING
 AERODYNAMICS
 DYNAMICS
 AEROTHERMODYNAMICS
 MATERIAL BEHAVIOR
 WISH TO MEASURE ABOVE, RELATE TO PREDICTIONS, AND IMPROVE
 SIMULATION MODELS

Figure 3. Instrumentation objectives.

Of course the methodology is to measure parameters that can be related to the predictions and then to improve the simulation models (codes/prediction). Offboard instrumentation (Fig. 4) is utilized to calculate aerodynamic parameters knowing the pressure,

	INSTRUMENT		MEASUREMENT TYPE
ATMOSPHERE	BALLONS, ROCKET	— —	WINDS, TEMP, DENSITY TEMP, DENSITY
DYNAMIC	RADAR, OPTICS	—	RANGE, AZIMUTH, ELEVATION

Figure 4. Offboard instrumentation.

temperature, and winds in the atmosphere (free-stream conditions). These measurements can be obtained from balloons or rockets launched just prior to or just after the flight test. The dynamics of the vehicle in terms of elevation, range, and position are measured on an instrumented range with radar and optics techniques. Onboard data are typically telemetered to the ground during the flight, and they include the instruments listed in Fig. 5. As can be seen, the list contains many complex "instruments," and a comprehensive discussion of this entire list is

	INSTRUMENT	MEASUREMENT TYPE
DYNAMIC	ACCELEROMETERS GYRO PLATFORM—COMPUTER MAGNETOMETER HIGH FREQUENCY ACCELEROMETER	ACCEL (3 AXIS) ANGLE RATES (3 AXIS) POS, VEL, ANGLE, ANGLE RATES ANGLE VIBRATION
AEROTHERMODYNAMICS	ACCOUSTIC NOSETIP BALANCE HINGE MOMENT STRAIN GAGE ACTUATOR PRESSURE	TRANSITION FORCE, MOMENT FORCE, MOMENT FORCE
	THERMOCOUPLES PHOTODIODES PYROMETERS CALORIMETERS	TEMP TRANSITION TEMP HEAT RATE
MATERIAL	ULTRASONIC RADIOACTIVE STRIP THERMOCOUPLE R.F. COUPLING	RECESSION RECESSION RECESSION ELECT CONDUCT

Figure 5. Onboard instrumentation.

far beyond the scope of this lecture series; however, we will focus on the aerothermodynamic techniques.

AEROTHERMAL OVERVIEW

Figure 6 outlines the methodology for the analytical and experimental approach to flight test aerothermal issues. The flight Reynolds number at which the boundary-layer transitions from laminar to turbulent can significantly influence vehicle design, since turbulent heating rates can be an order of magnitude higher than the laminar values. Unfortunately, the ability to predict boundary-layer transition

USE TRAJECTORY, ATTITUDE, TRANSITION CRITERIA, AND GEOMETRY TO PREDICT SURFACE HEATING RATES

USE HEATING RATES AND MATERIAL MODELS TO PREDICT INDEPTH TEMPERATURES

COMPARE PREDICTED AND MEASURED HEATING RATES/TEMPERATURE DATA

ADJUST HEATING MODEL TO BEST MATCH PREDICTIONS AND DATA

COMPARE ABLATION PREDICTIONS WITH RESSION MEASUREMENTS

Figure 6. Flight test aerothermal methodology.

continues to elude the aerodynamicist. This subject will be discussed in more detail later in these notes. Heating rate measurements versus temperature measurement is often an issue because of the limited number of channels available during the flight. In general, the pros and cons of this issue are listed in Fig. 7 and a specific example of this issue will be presented below. However, we shall first address a typical flight test scenario.

- FLIGHT SYSTEMS ENGINEER LIMITS AEROTHERMAL CHANNELS
- HEAT RATE VS. TEMPERATURE ("ONE OR THE OTHER")

—BUT NEED BOTH FOR EACH GAGE

$$\dot{q} = h(T_s - T_w)$$

	PROS	CONS
HEAT RATE ONLY	BASIC INPUT PARAMETER FOR CODE THERMAL ANALYSIS	DOESN'T ANSWER—DO COMPONENTS GET TOO HOT
TEMPERATURE ONLY	ANSWERS FUNDAMENTAL ISSUE DO COMPONENTS GET TOO HOT	NOT BASIC PARAMETER: $f(\dot{q})$ POOR ANALYSIS PARAMETER: $f(\text{CONDUCTION, RADIATION, CONVECTION, SPECIFIC FLIGHT})$
RECOMMEND	COMPLETE SET OF DATA FOR HEAT RATE AND TEMPERATURE INPUTS FOR THERMAL ANALYSIS AND TO ANALYZE FLT DATA ANOMALIES	REQUIRES MORE DATA CHANNELS

Figure 7. Data channel limitations.

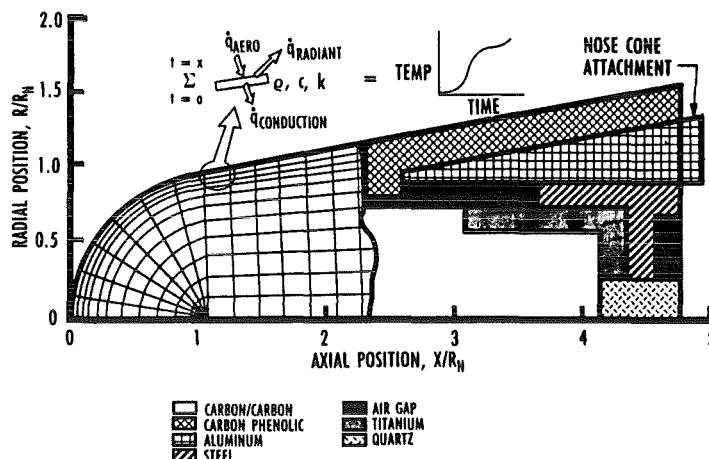


Figure 8. Illustration of finite element model.

The particular example to be addressed concerns the analysis of a nose cone constructed of a variety of materials but anchored to the cone frustum by aluminum as shown in Fig. 8. A specific question which needs to be answered is, "Will the Al exceed its critical temperature (283°C, 1,000°R) during the flight?" In general, all three modes of heat transfer need to be analyzed:

— Convection [aeroheating $\approx f(M_\infty, R_\infty, \text{geom})$]

— Radiation {from (or to) the surface $\approx f(T_w^4, \epsilon)$ }

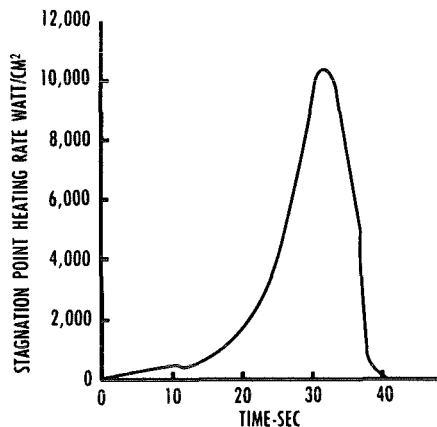
— Conduction [from surface to Al $\approx \frac{\partial T_w}{\partial x}, q, c, k$]

The conduction analysis is typically accomplished by a finite-element code illustrated in Fig. 8 which solves the heat conduction equation for each element (knowing q, c, k) as the vehicle descends along the flight trajectory.

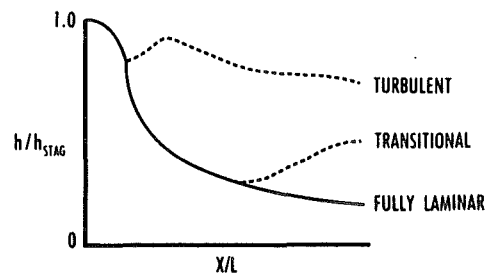
The aeroheating input (\dot{q}_{AERO}) is typically calculated at the hemispherical stagnation point² along the flight trajectory as illustrated in Fig. 9a. This parameter is often used as a reference value to nondimensionalize the heating distribution of the remainder of the configuration (e.g., h/h_{STAG}). Of course, the distribution over the configuration continually changes with Mach number, Reynolds number, and boundary-layer state (laminar versus turbulent), as can be seen in Fig. 9b. One example of the results of this analysis is shown in Fig. 10, which presents isotherm (constant temp) lines at the specific instant noted during the flight. As can be seen the Al component approaches 283°C; however, this particular design appears to do an excellent job of spreading the heat load.

HEAT GAGE INTEGRATION INTO STRUCTURE

An analysis similar to that presented above was performed for the flight test vehicle illustrated in Fig. 11. As can be seen, 14 heat flux gages were installed in this particular vehicle. The desired characteristics of flight test heat flux instrumentation are:



a. Stagnation point heating



b. Distribution along body as a function of boundary layer state

Figure 9. Illustration of aeroheating during reentry.

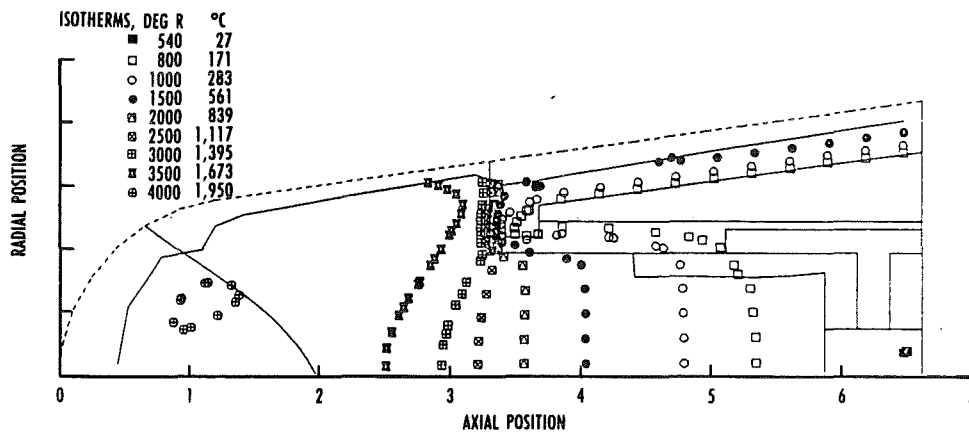


Figure 10. Test case nosetip analysis isotherm predictions.

- Output proportional to heat flux (\dot{q}) as opposed to inferring \dot{q} from temperature measurements (e.g., "coax gage")
- Complete integration of "gage" into vehicle surface so that the thermal response of "gage" and surrounding are identical
- Output of both \dot{q} and "gage" temperature should be available

The Schmidt-Boelter gage³ has some of these characteristics and was the type gage used on the configuration shown in Fig. 11. Typical resulting data for a representative gage are presented in Fig. 12. The disagreement between the data and the prediction (≈ 30 percent at about 45 sec) for this gage is not only representative of **all** gages on this vehicle, it is also typical of other heat rate flight data (see Refs. 4 and 5 for other similar discussions). It is important to

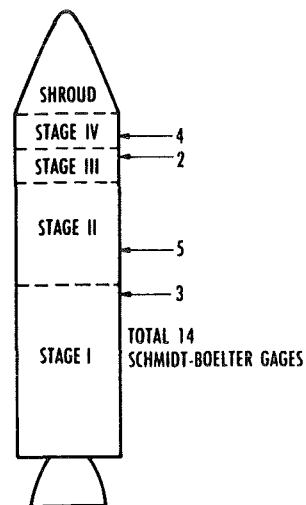


Figure 11. Approximate locations of heat-flux gages on flight test missile.

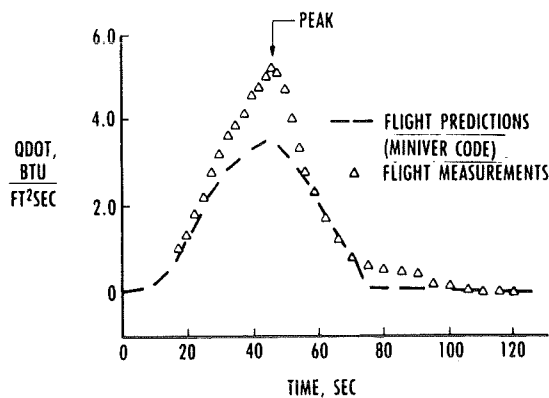


Figure 12. Typical flight test heating rate data.

recognize the three possibilities when the data and predictions don't agree:

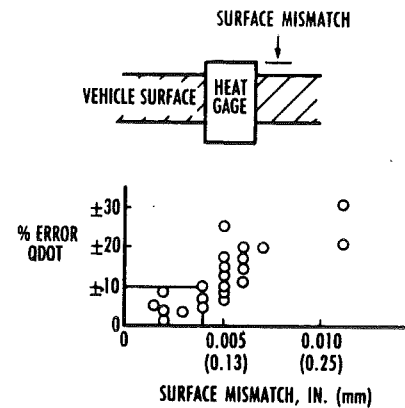
- Predictions incorrect
- Data incorrect
- both incorrect

A list of some (not all) of the possible reasons for incorrect flight heat rate measurements for this case is shown in Fig. 13. Experience has shown that numbers 1 and 2 are very common, unfortunately. Figure 14 illustrates the importance of a good gage "fit" into the surface such that the gage is flush within 0.004 in. (0.10 mm).

- HEAT RATE INSTRUMENTATION APPLICATION VIOLATES GAGE "PRINCIPLE OF OPERATIONS"
- POOR GAGE INSTALLATION
- INACCURATE HEAT-FLUX GAGE TEMPERATURE PREDICTIONS
- NONISOTHERMAL WALL EFFECT
- AEROHEATING PREDICTIONS NEGLECT PLUME INTERFERENCE EFFECT ON FLOW FIELD
- CALIBRATION SHIFT
- INACCURATE FACTORY CALIBRATIONS
- SENSOR SURFACE DAMAGE
- FLIGHT DATA SYSTEM ERRORS
- FLIGHT VEHICLE SURFACE ABLATION/EROSION OR DISTORTION
- GAGE FAILED PREFLIGHT AND/OR POSTFLIGHT OPERATIONAL CHECKOUT

Figure 13. Possible problem areas in flight measurements.

Integration of the gage into the vehicle surface has been discussed at great length by Neumann and others.



- TO MAINTAIN ERROR < 10% MISMATCH ≤ 0.004 IN. (0.10 mm)
- GAPS BETWEEN GAGE AND SURFACE PROMOTE SIMILAR ERRORS

Figure 14. Heat gage installation effects.

For the present example, Fig. 15 shows the mismatch between the gage material and the surrounding material, VAMAC (a rubber insulator). Mismatched material can cause significant nonisothermal wall effects (see Fig. 16), and since \dot{q} is a strong function of wall temperature the measured heating rates are significantly affected. Unfortunately, neither the gage nor the VAMAC temperature was measured during this flight test. For the flight data previously presented in Fig. 12 and the gage installation shown, estimates were made of the thermal response (temperature) of both the gage and the surrounding surface (see Fig. 17).

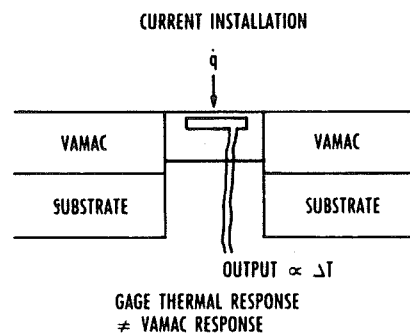


Figure 15. Mounting gages in insulative surface can produce errors in flight test data.

Recalling from Fig. 12 that peak heating occurred at about 45 sec, we see that this corresponds to a calculated mismatch in temperature of about 135°F (57°C). Applying the methods used by Prakaraj,⁵ the nonisothermal wall effects can be accounted for, and corrections to the measured flight data can be made as shown in Fig. 18. For this case the peak heating

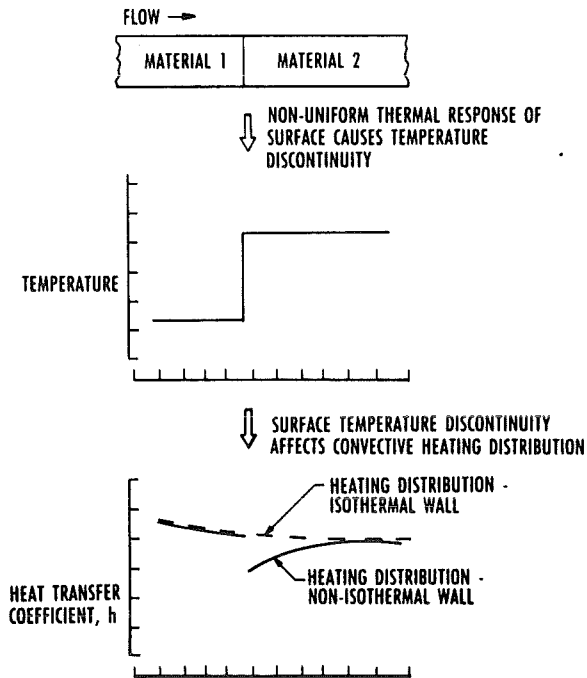


Figure 16. Non-isothermal wall affects convective heating.

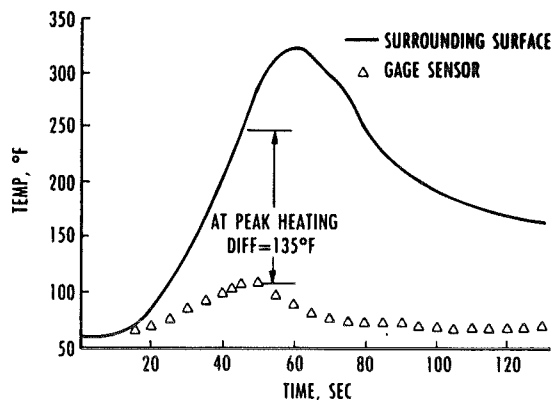


Figure 17. An example of thermal analysis predictions.

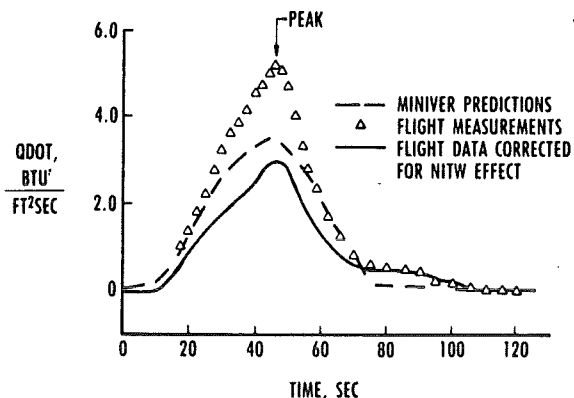


Figure 18. An example of calculated non-isothermal wall (NITW) effect.

- "GAGES" SHOULD BE PLANNED VERY EARLY IN PROGRAM AND REQUIRE INTEGRATION INTO STRUCTURE WHICH MUST BE VERIFIED BY DETAIL THERMAL ANALYSIS
- USE HEAT FLUX GAGES INSTRUMENTED WITH THERMOCOUPLES (NEED BOTH \dot{q} AND T_w)
- MONITOR HEAT GAGE INSTALLATION AND INSURE STRICT "FLUSHNESS" SPECIFICATION,
- GROUND TEST CHECK-OUT OF FLIGHT TEST INSTRUMENTATION IN SIMULATED ENVIRONMENT

Figure 19. Some specific recommendations.

value was reduced from 5.2 to 2.9 Btu/ft²-sec (44 percent). This type of "correction" to the flight data is highly undesirable, but unfortunately it is not uncommon. The solution to this problem is to start very early in the program to "design in" the desired heat flux instrumentation so that the "gage" is integrated into the surface and has the same thermal response as the surface (i.e., no temperature mismatch). This example also illustrated the importance of wall temperature measurements to complement the heat rate measurements. Most heat rate gages can be purchased with installed thermocouples for gage surface temperature measurements. This is highly recommended because, without this information data anomalies cannot be resolved. Additional specific recommendations are presented in Fig. 19.

REFERENCES

1. Williamson, W. E. "Hypersonic Flight Testing." Hypersonics Short Course, The University of Texas at Austin, April 1987.
2. Fay, J. A. and Riddell, F. R. "Theory of Stagnation Point Heat Transfer in Dissociated Air." *Journal of Aerospace Sciences*, Vol. 25, No. 2, pp. 73-85, 121, February 1958.
3. Kidd, C. T. "A Durable, Intermediate Temperature, Direct Reading Heat Flux Transducer for Measurements in Continuous Wind Tunnels." AEDC-TR-81-19 (AD-A107729), November 1981.
4. Neumann, R. D. "Designing A Flight Test Program." 1st Joint Europe-US Short Course on Hypersonics, The University of Texas at Austin, April 1987.
5. Praharaj, S. C. and Foster, L. D. "Orbital Flight Test Shuttle External Tank Flowfield and Aerothermal Analysis." AIAA 84-1750, 1984.

EXTRAPOLATION OF GROUND TEST DATA TO FLIGHT

by

JAMES R. MAUS

Principal Engineer

Calspan Corporation/AEDC Operations

Arnold Engineering Development Center

ABSTRACT

The initial flights of the Space Shuttle uncovered a number of differences between pre-flight aerodynamic predictions and actual flight data. Most notable among these discrepancies was for longitudinal trim during high speed re-entry. To investigate these differences, several computer codes were applied to a modified Space Shuttle Orbiter to determine aerodynamic parameters over a wide range of conditions. Computations were carried out for wind tunnel conditions and flight conditions to assess Mach number, real gas, and viscous effects on the reentry aerodynamics of the orbiter. Based on the CFD results and a semi-empirical analysis of viscous effects, an aerodynamic model for the orbiter was developed to extrapolate wind tunnel data for the Space Shuttle Orbiter to flight conditions.

NOMENCLATURE

Latin

A	Reference area, 250 m ²
a	Speed of sound
BF	Body flap deflection, deg.
C _A	Axial-force coefficient, F_A/Aq_∞
C _M	Pitching-moment coefficient, M_o/cAq_∞
C _N	Normal-force coefficient, F_N/Aq_∞
C _p	Pressure coefficient, $(P - P_\infty)/q_\infty$
C _∞	Chapman-Rubens constant, $\mu_w T_\infty / (\mu_\infty T_w)$
CG	Center of gravity
c	Reference length, 12.06 m
F _A	Axial force component
F _N	Normal force component
L	Body length, 32.84 m
M _∞	Free-stream Mach number, V_∞/a_∞
M _o	Total moment about X _o = 21.35 m, Z _o = 0.94 m

P	Pressure
\dot{Q}	Surface heat transfer rate
q _∞	Dynamic pressure, $\rho_\infty V_\infty^2/2$
Re	Free-stream Reynolds number/m or as noted
Re _{∞L}	Free-stream Reynolds number based on vehicle length
V	Velocity
\overline{V}_∞	Viscous interaction parameter, $M_\infty \sqrt{C_\infty} / \sqrt{Re_{\infty L}}$
X _{CP}	Center-of-pressure location
x,y,z	Cartesian coordinates
Greek	
α	Angle-of-attack
γ	Specific heat ratio
δ	Deflection angle
Δ	Difference or increment
μ	Dynamic viscosity

INTRODUCTION

No ground test facility can reproduce all of the flow parameters required to fully simulate high-velocity reentry flight. Yet, the effects of high Mach number, high enthalpy flow on vehicle aerodynamics must be accounted for if large uncertainties in the stability and performance of reentry vehicles are to be avoided. At Arnold Engineering Development Center, several analysis programs have been concerned with the extrapolation of ground test data to hypersonic flight conditions. The most recent and most extensive of these has been for the reentry of the space shuttle orbiter.

The space shuttle orbiter is a highly maneuverable vehicle. A gliding reentry from orbital velocity to a horizontal landing on conventional runways is made possible by the aerodynamics generated by a double

delta planform and both body flap and wing elevon controls. The body flap is the predominant longitudinal trim device, while the wing-mounted elevons are used for longitudinal control and as ailerons for lateral control. The overall dimensions of the orbiter are given in Fig. 1.

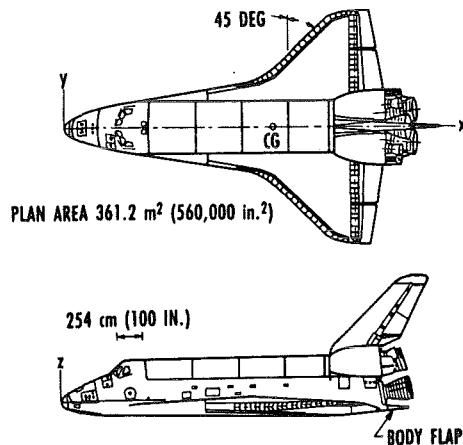


Figure 1. Space shuttle orbiter geometry.

Although the reentry phase of the space shuttle flight test program was remarkably successful, a number of discrepancies between preflight predictions of aerodynamics and flight data were uncovered. Most notable among these was in the area of longitudinal trim at high Mach numbers. At these hypersonic conditions, much greater control surface deflections than predicted prior to flight, were required to maintain proper vehicle attitude because of the misprediction of the pitching moment.¹ The results of these mispredictions are illustrated in Figs. 2 and 3.

The preflight predictions of the orbiter aerodynamics were based primarily on ground test data obtained in a very extensive wind tunnel test program, the most extensive in aviation history. This paper describes a study carried out at Arnold Engineering Development Center to attempt to resolve discrepancies between the space shuttle orbiter wind tunnel and flight data, and to provide a rational basis for extrapolating ground test data to hypersonic flight conditions.

APPROACH

In general, wind tunnel data cannot be used directly for predicting the aerodynamic characteristics of a vehicle in hypersonic flight. Continuous flow or blowdown facilities which yield the highest quality data cannot achieve the Mach numbers associated

with reentry flight. Moreover, the high temperatures experienced in hypersonic flight cause air to depart substantially from ideal gas behavior, a situation that cannot be adequately simulated in wind tunnels. These and many other severe simulation problems limit the applicability of ground test facilities in the hypervelocity regime.

The approach taken during this study was to couple a set of high-quality wind tunnel data² with computational fluid dynamic solutions for high Mach number flight conditions. The CFD codes were used to extend the wind tunnel data to hypervelocity conditions taking into account Mach number, real gas, and viscous effects on the aerodynamics of the orbiter.

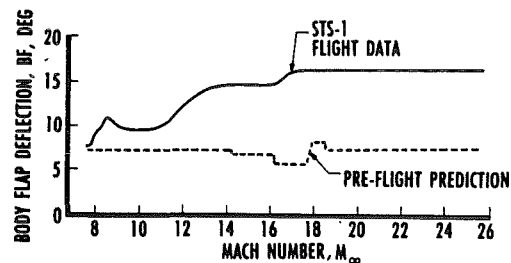


Figure 2. Comparison of STS-1 flight data with prediction.

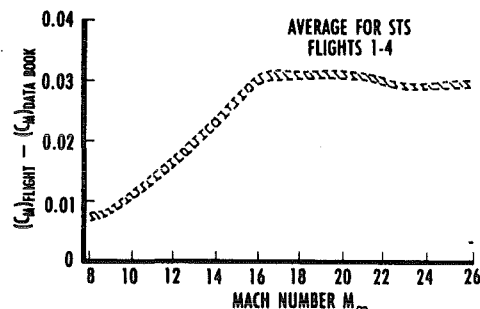


Figure 3. Difference in pitching-moment coefficient.

To assess the influence of high Mach number and real-gas effects on the space shuttle orbiter aerodynamics during reentry, inviscid CFD codes were applied to a modified orbiter configuration. Detailed flow-field solutions were obtained for both wind tunnel conditions and flight conditions and computed surface pressures were integrated over the body to determine the aerodynamic forces and moments acting on the vehicle. Perfect-gas computations at $M_\infty = 8$ were used as baseline conditions from which the change in aerodynamic coefficients due to high Mach numbers and real-gas effects were measured. The $M_\infty = 8$ computations were also

compared with aerodynamic and pressure data^{2,3} from AEDC Tunnel B on a 0.0175-scale, high-fidelity model to validate/calibrate the computational results.

Viscous effects on orbiter aerodynamics were pursued using CFD solutions as well as an analysis of experimental data leading to simple analytic expressions for viscous contributions to C_A and C_M .

The majority of the work discussed herein concerns Mach number, real-gas, and viscous effects on the aerodynamics of the basic orbiter configuration. These appear to be the principal cause of the misprediction. However, there is also evidence of degradation of control effectiveness, and a later section discusses this aspect of the problem.

INVISCID COMPUTATIONS

The geometry used for the inviscid computations is illustrated in Fig. 4. This configuration was generated with the Grumman QUICK geometry modelling program⁴ and was obtained from NASA LaRC. The model has been used extensively in orbiter studies and was not altered during the present investigation. The major difference between the computational model geometry and the actual orbiter are as follows: (1) the wing sweep back angle has been increased from 45 to 55 degs; (2) the wing thickness of the model is about twice that of the orbiter; (3) the canopy has been smoothed out; (4) the rudder and OMS pods were not included in the model geometry; and (5) the computational geometry is squared off at the body flap hinge line. These modifications to the geometry were designed to avoid embedded subsonic flow regions at the wing-body junction, to remove the canopy shock, and to avoid the complex lee side flow features that have little influence on the aerodynamics at high angle of attack. The projected planform area is approximately 2 percent less than the orbiter projected area, and the centroid of the projected area is approximately 2 percent of model length further aft than for the orbiter. For consistency, however, the actual orbiter wing area and mean aerodynamic chord were used in calculating all aerodynamic coefficients.

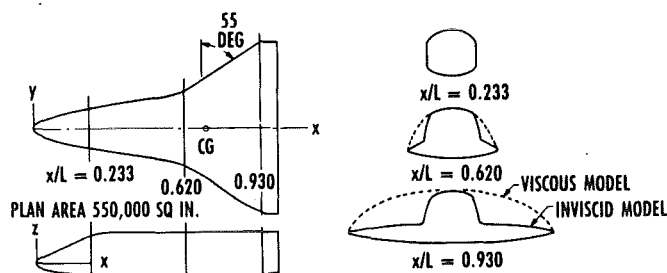


Figure 4. Computational model geometry.

Computer Codes

The inviscid computer codes used to determine Mach number and real-gas effects were CM3DT⁵ and STEIN⁶. CM3DT is a three-dimensional, time-marching Euler solver that is used to provide a starting solution for the supersonic space-marching code STEIN, which was applied over the major portion of the vehicle. The regions for which the codes were used are illustrated in Fig. 5. CM3DT and STEIN are each interfaced with the QUICK geometry routines which specify the body shape and compute geometrical parameters on the surface. Both codes employ conformal mapping to transform the physical space between the body and the bow shock into a rectangular computational domain.

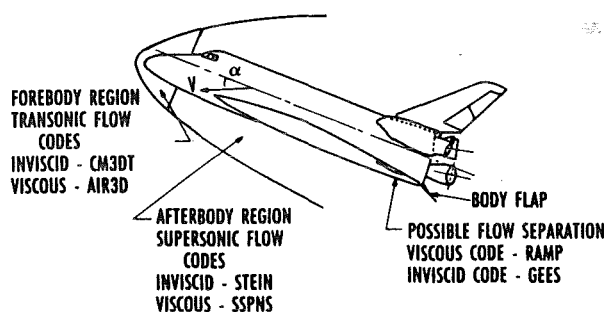


Figure 5. Computational regions of various codes.

Both CM3DT and STEIN can be used either for perfect-gas or equilibrium air computations. Tabulated thermodynamic properties, in conjunction with table look-up routines, are used for equilibrium air computations.

Comparison with Wind Tunnel Data

To establish credibility of the CFD results and to assess the effect of geometrical differences on the

aerodynamic parameters, initial computations with CM3DT and STEIN were made to compare with wind tunnel results. The specific wind tunnel data used in these comparisons are from AEDC Tunnel B,^{2, 3}

Figure 6 shows a comparison of computed and measured pressure coefficients along the windward centerline at $M_\infty = 8.0$ for two angles of attack. The computed pressure distributions, although slightly overpredicting the pressures in the mid-body region, generally agree very well with the experimental values. Pitot profile data taken along the windward centerline allow comparison of the boundary-layer edge Mach number with the surface Mach number computed with STEIN. This comparison is shown in Fig. 7 for an angle of attack of 30 deg. Also shown on this figure are surface Mach number distributions determined from the pressure data for two extreme assumptions on entropy swallowing: (1) a boundary layer of zero thickness, and (2) a fully viscous shock layer with edge conditions given by local tangent cone theory.

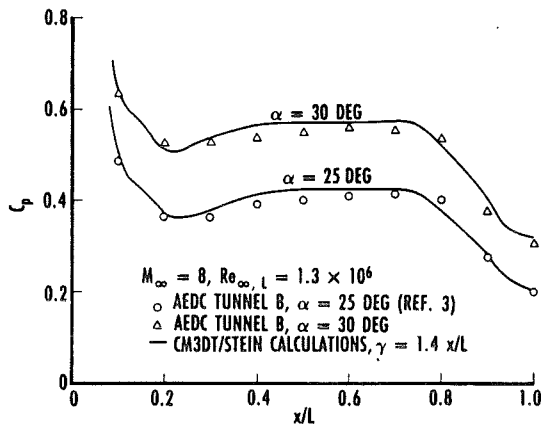


Figure 6. Comparison of computed pressure distributions on windward centerline with experimental data.

A comparison of computed and experimental normal-force coefficients is shown in Fig. 8. The reference area used to nondimensionalize the calculated value is the actual orbiter wing area, $A_{REF} = 250 \text{ m}^2 \text{ ft}^2$. The agreement shown would be improved were the reference area reduced by 2 percent to account for differences in the projected planform area.

Predicting pitching moment is a severe test of any CFD code. Figure 9 shows a comparison of com-

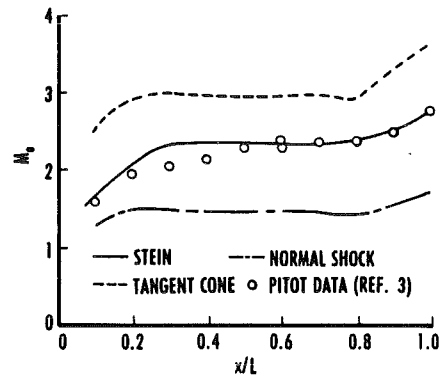


Figure 7. Comparison of computed edge Mach number with experimental data.

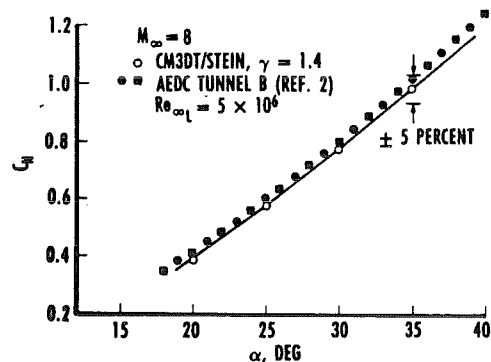


Figure 8. Comparison of computed normal-force coefficient with experimental data.

puted pitching-moment coefficient with experimental values for the basic orbiter geometry. The maximum deviation, which occurs at an angle of attack of about 30 deg, corresponds to a difference of center of pressure of 0.3 percent of the body length.

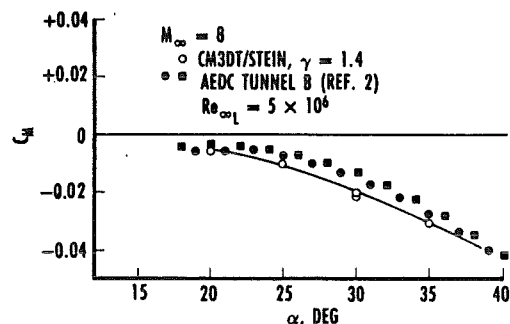


Figure 9. Comparison of computed pitching-moment coefficient with experimental data.

The results of the above comparisons, in addition to giving confidence in the applicability of the

computational codes to the complex orbiter model geometry, also indicate that there are no great aerodynamic differences between the computational geometry and the actual orbiter geometry for these high Mach number test conditions.

Mach Number and Real-Gas Effects

Changes of the orbiter aerodynamics from the baseline conditions due to hypersonic Mach number and equilibrium air thermodynamics were investigated by carrying out a series of CFD computations using CM3DT and STEIN. Computations were made for the matrix of conditions shown in Table 1. As indicated in this table, difficulties were encountered in obtaining solutions at the highest angle of attack. Nonetheless, it is believed that the consistency of the results is such that values at higher angle of attack can be extrapolated without great risk.

Table 1. Matrix of Conditions for Inviscid Computations.

α , DEG	GAS	MACH NUMBER				
		8	13	18	23	
20	IDEAL	v	v	v	v	v - COMPUTATION v - COMPLETED x - COMPUTATION FAILED
	REAL	v	v	v	v	
25	IDEAL	v	v	v	v	
	REAL	v	v	v	v	
30	IDEAL	v	v	v	v	
	REAL	v	v	v	v	
35	IDEAL	v	v	v	v	
	REAL	v	v	v	v	
40	IDEAL	x	v	v	v	
	REAL	x	x	x	x	

REAL-GAS CONDITIONS

$M_\infty = 8$ $V_\infty = 2622$ m/sec (8600 ft/sec) Altitude = 46.3 km (152,000 ft)
 $M_\infty = 13$ $V_\infty = 4268$ m/sec (14,000 ft/sec) Altitude = 57.3 km (188,000 ft)
 $M_\infty = 18$ $V_\infty = 5488$ m/sec (18,000 ft/sec) Altitude = 64.6 km (212,000 ft)
 $M_\infty = 23$ $V_\infty = 6707$ m/sec (22,000 ft/sec) Altitude = 73.2 km (240,000 ft)

Mach Number Effects

Figure 10 compares pressure coefficient distributions along the windward centerline of the model orbiter geometry for two angles of attack and Mach numbers of 8.0 and 23.0. The results in this figure were obtained assuming flow of an ideal gas with $\gamma = 1.4$. These results show that increasing Mach number causes a slight decrease in pressure coefficient over the entire body, a trend that is consistent with supersonic flow over cones and wedges.

The effect of Mach number variations on the aerodynamic coefficients C_A , C_N , and C_M is shown in Figs. 11, 12, and 13, respectively. Both the axial- and normal-force coefficients show a decrease with

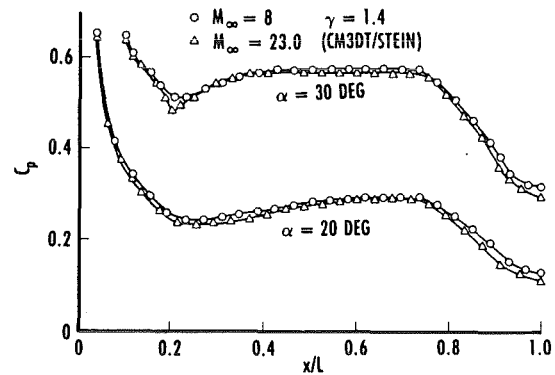


Figure 10. Effect of Mach number on windward centerline pressure distributions.

increasing Mach number due to the decreased pressure coefficients. The pitching-moment coefficient increases (more nose up) with Mach number due to the decrease of pressure coefficient in the aft portion of the vehicle, where the area is concentrated. The increase in pitching moment is most pronounced at low angles of attack. As expected, all three coefficients asymptotically approach constant values as the Mach number becomes large.

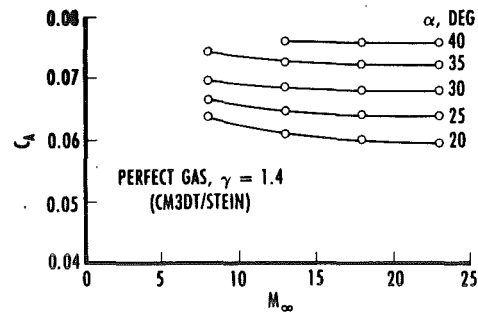


Figure 11. Effect of Mach number on axial-force coefficient.

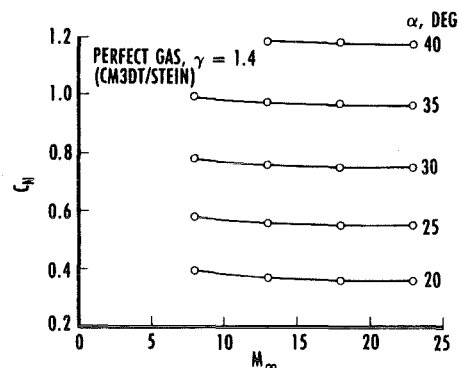


Figure 12. Effect of Mach number on normal-force coefficient.

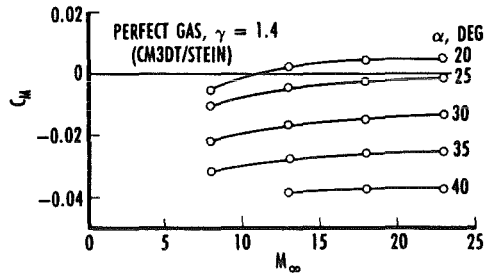


Figure 13. Effect of Mach number on pitching-moment coefficient.

Figure 14 shows the forward shift in center of pressure from the reference condition at $M_\infty = 8.0$ as a function of Mach number and angle of attack. This figure indicates a substantial shift forward in center of pressure at lower angles of attack due to Mach number.

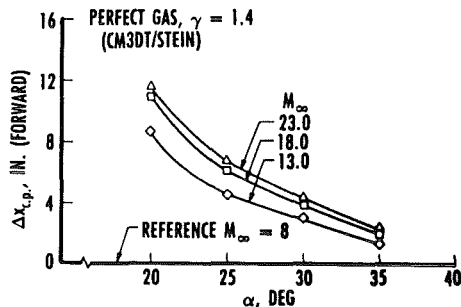


Figure 14. Effect of Mach number on center-of-pressure location.

Real-Gas Effects

The effect of equilibrium chemistry on the aerodynamics of the Orbiter were examined by comparing inviscid computational results obtained with CM3DT and STEIN for a perfect gas with $\gamma = 1.4$ to results at similar conditions for equilibrium air. The most dramatic effects of equilibrium air occur within the wind side shock layer and are illustrated in Figs. 15-17. Figure 15 shows comparative wind side shock shapes at Mach 23 and 35-deg angle of attack. A small influence on the pressure and velocity distributions through the shock layer is shown in Fig. 16. Comparative profiles of Mach number and temperature given in Fig. 17 show the greatest change. The value of the isentropic exponent through the shock layer at $x/L = 0.775$ is $\gamma_e = 1.137$.

The effect of real-gas thermodynamics on the surface pressure distribution is illustrated in Figs. 18 and 19 by comparing the pressure distribution for a

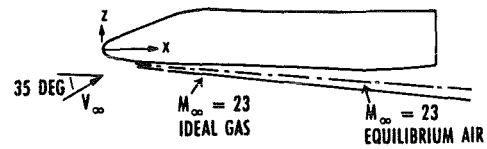


Figure 15. Comparative shock shapes.

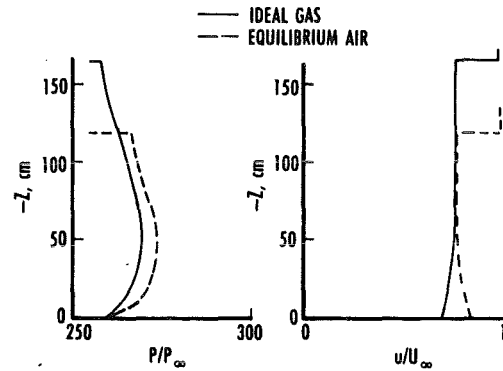


Figure 16. Shock layer pressure and velocity profiles.

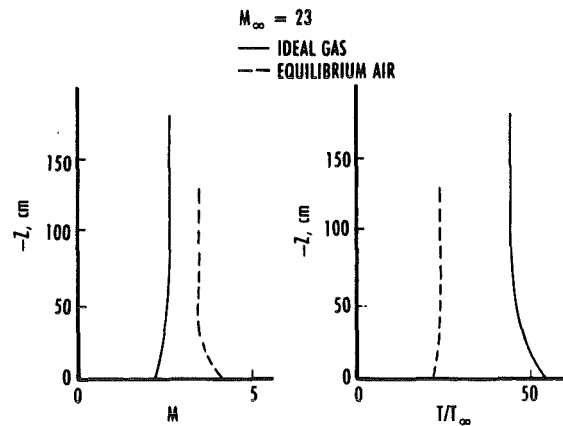


Figure 17. Shock layer Mach number and temperature profiles.

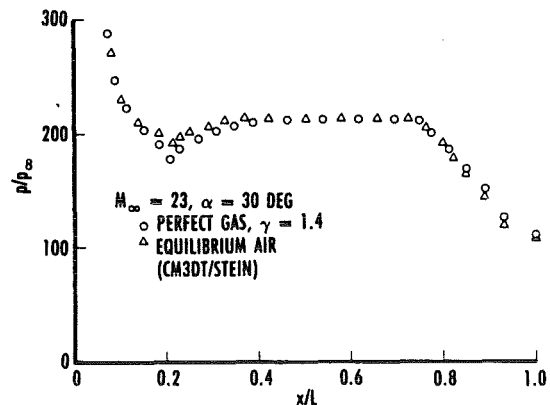


Figure 18. Real-gas effect on windward centerline pressure distribution.

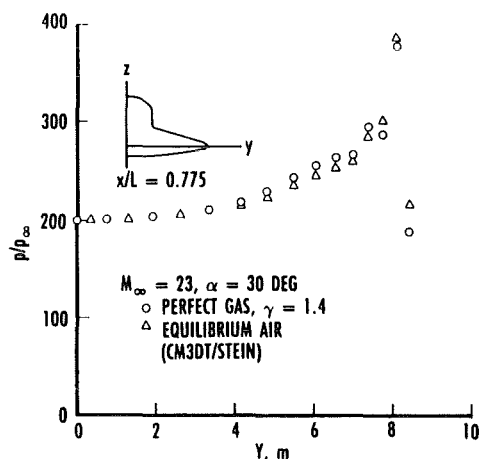


Figure 19. Real-gas effect on aft windward pressure distribution.

perfect gas at Mach 23 with an equilibrium air computation at approximately the same Mach number. Figure 18 shows comparative pressures along the windward centerline. Note that the real-gas pressure is slightly higher than perfect-gas pressure in the forebody region and somewhat lower on the afterbody. These distributions indicate that an effect of equilibrium air will be to produce a more positive (nose up) pitching moment. Figure 19 compares span-wise pressure distributions at $x/L = 0.775$ and shows that the real-gas effects cause a reduced pressure over most of the aft windward portion of the body, but an increase near the leading edge.

Considering that a major factor in the real-gas influence on aerodynamics is through a reduction in the effective gamma, one can show the trends exhibited by the pressure distributions are consistent with simple relations from hypersonic flow theory. The Rayleigh pitot formula, for example, shows that at constant Mach number, the stagnation point pressure increases with decreasing gamma. Tangent cone or tangent wedge theory, on the other hand, applied to the afterbody region shows a decrease in pressure coefficient with decreasing gamma.

Real-gas effects on the axial- and normal-force coefficients of the orbiter model geometry are illustrated in Figs. 20 and 21. Figure 20 demonstrates that the real-gas effects increase the axial-force coefficient. This is attributed to the higher pressures on the forebody and wing leading edges shown previously. Figure 21 indicates a slight decrease in normal force due to lower pressure on the aft portion of the vehicle.

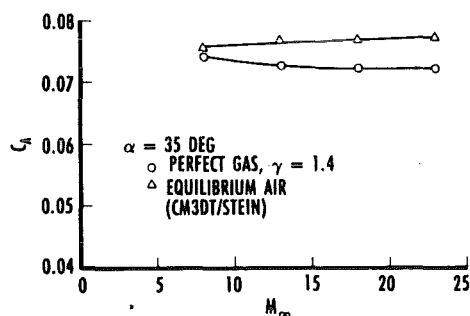


Figure 20. Real-gas effect on axial-force coefficient.

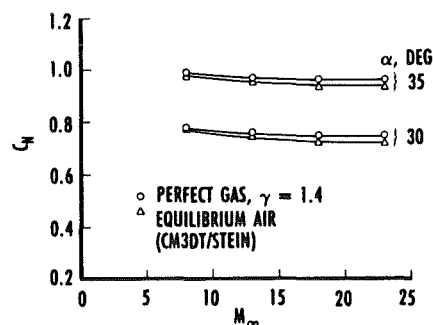


Figure 21. Real-gas effect on normal-force coefficient.

Real-gas effects on pitching moment are shown for the high-velocity, high altitude case in Fig. 22 by comparing the results for perfect-gas computations with those for equilibrium air thermodynamics. This figure reveals that the real-gas effects tend to drive C_M more positive with the effect being most significant at higher angles of attack. As angle of attack increases, the effective bluntness of the vehicle becomes greater, producing a stronger bow shock.

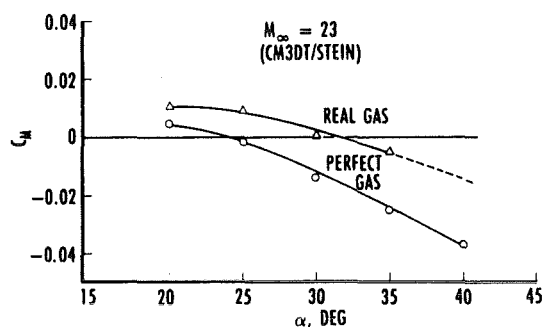


Figure 22. Real-gas effect on pitching-moment coefficient.

Combined Mach Number and Real-Gas Effects

Combined Mach number and real-gas effects are shown in Fig. 23 for the high Mach number

condition, in terms of forward shift in center of pressure from the baseline Mach 8, perfect gas case. The relatively large shift at low angles of attack is, in part, due to a reduced C_N , making the center-of-pressure location very sensitive to changes in C_M .

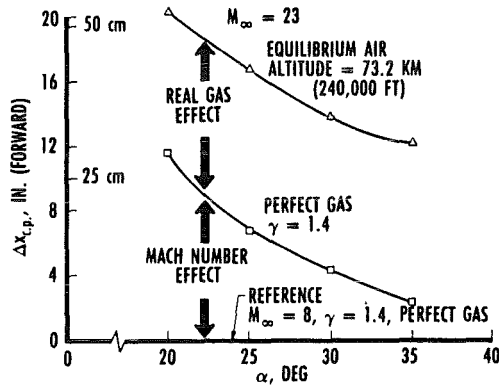


Figure 23. Combined Mach number and real-gas effects on center-of-pressure location.

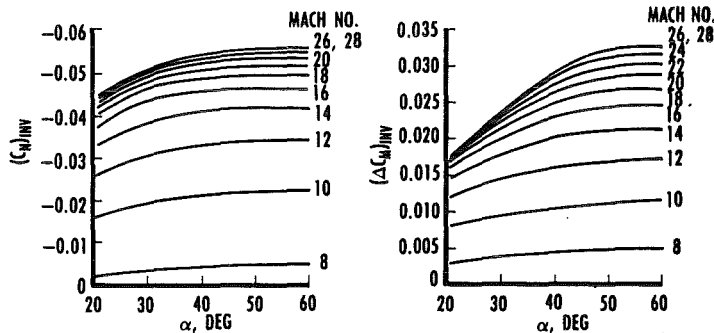


Figure 24. Combined Mach number and real-gas effects on aerodynamic coefficients C_N and C_M .

The combined corrections of C_N and C_M due to Mach number and real-gas effects, based on inviscid computations, are shown in Fig. 24 as a function of Mach number and angle of attack. Engineering judgment was used in fairing the curves and extrapolating outside the computational database. Note the following: (1) at high angles of attack and high Mach numbers, the shift in C_M of about 0.030 due to Mach number and real-gas effects; (2) there is a loss of normal force due to these effects; and (3) there is a small effect at Mach 8.

Additional details on the inviscid computational results can be found in Ref. 7.

VISCOUS ANALYSIS

The analysis of the viscous effects on the space shuttle orbiter aerodynamics was pursued using two

complementary approaches: (1) fully viscous computations for a modified orbiter geometry using a parabolized Navier-Stokes computer code, and (2) the development of simple analytical expressions for the viscous contributions to C_A and C_M from theoretical considerations and experimental data.

Computational Study

The principal effort in this part of the program was to obtain laminar viscous flow-field solutions for a model orbiter using existing computer codes. The model geometry used for these computations is similar to that employed for the inviscid computations. The principal difference between the two models is that the upper surface of the viscous geometry is approximated by ellipses as shown by the dashed lines in Fig. 4.

Computer Codes

The computer programs used for the viscous computations were two codes developed principally at NASA Ames based on an implicit, approximately factored, finite difference solution (Beam and Warming algorithm) of the thin-layer Navier-Stokes equations. The blunt body code, AIR3D, is a three-dimensional, time-dependent Navier-Stokes solver developed by Pulliam and Steger.⁸ Bow shock fitting and other refinements were added to the code by Kutler, et al.⁹

This code is applied far enough back on the body that the flow outside the boundary layer is fully supersonic. At this location, a starting plane is generated for the supersonic space-marching afterbody code.

The parabolized Navier-Stokes (PNS) code used for the viscous afterbody computations was originally developed in shock capturing form by Schiff and Steger¹⁰ and was modified by Chaussee, et al.¹¹ to include bow shock fitting. In structure, the code is very similar to the blunt body code with the axial independent variable assuming a time-like character is supersonic flow. Further development of this code was sponsored by the U. S. Air Force Wright Laboratory.¹²

At the time this work was being carried out, both codes were restricted to perfect-gas computations.

Obtaining PNS solution on the shuttle-like geometry was not an easy task. A number of modifications to the code, described in more detail in Ref. 13, were required to march the solution to the end of the body. In particular, severe problems were encountered at about $x/L = 0.6$, where the wing flare occurs. At this point it was necessary to discontinue the lee-side flow-field computations, introducing an artificial boundary condition just above the wing. With this change, the solution on the windward side could be continued to the end of the body for low angles of attack ($\alpha \approx 20$ deg).

Computational Results

Numerical solutions of the three-dimensional parabolized Navier-Stokes equations were obtained for the model geometry at $M_\infty = 23$ over a range of altitudes from 52 km to 86 km at an angle of attack of 20 deg. The orbiter angle of attack at these altitudes is about 40 deg, a much more difficult computation. A partial solution ($x/L < 0.6$) was also obtained at Mach 8 and 25 deg angle of attack. Free-stream conditions for the viscous computational cases are given in Table 2.

Table 2. Viscous Test Case Conditions.

	CASE				
	1	2	3	4	5
α , DEG	25	20	20	20	20
M_∞	7.92	23.0	23.0	23.0	23.0
T_∞ , K	52.7	234	234	234	234
T_w , K	300	1111.1	1111.1	1111.1	1111.1
Re , m^{-1}	18.23×10^5	7.87×10^4	1.57×10^4	3.02×10^3	3.93×10^4

Figure 25 presents the surface pressure results along the windward and leeward pitch planes of symmetry for two different Reynolds numbers. Also shown in this figure are STEIN results for the same geometry, Mach number, and angle of attack. As expected, the PNS results approach the inviscid computations as the Reynolds number increases. Note that the pressure on the lee side aft of $x/L = 0.2$ is very low, and should have little effect on the aerodynamic coefficients.

A comparison of computed heat-transfer distribution along the windward centerline with data from AEDC Tunnel B¹⁴ is presented in Fig. 26. The PNS code slightly overpredicts the data, but the agreement is considered good.

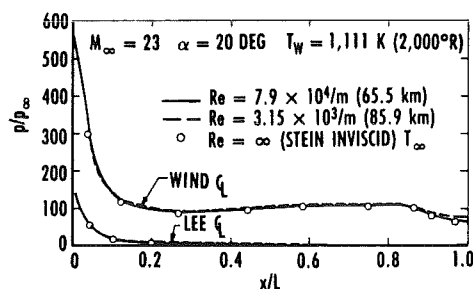


Figure 25. PNS computations of surface pressure distribution.

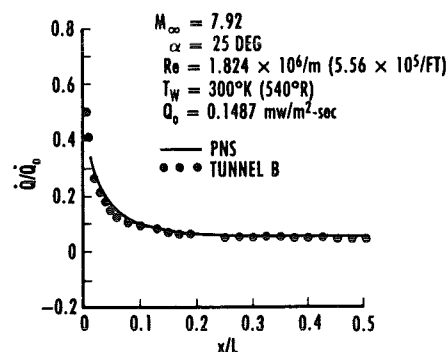


Figure 26. PNS results for heat transfer on wind-side pitch plane compared with experimental data.

Figure 27 shows the axial-force coefficients, C_A , and pitching moment coefficient, C_M , computed at $\alpha = 20$ deg, plotted against viscous interaction parameter, \bar{V}_∞ . All of the results shown in this figure were obtained at $M_\infty = 23$, varying Reynolds number to simulate different altitudes of the re-entry trajectory. Pressure and viscous forces were integrated individually to separate induced pressure contributions from viscous shear. The unrealistically high C_A levels are due to the large pressure drag on the very blunt-winged computational model.

Approximate Expressions

Simple approximate analytical expressions for the viscous contributions to C_A and C_M have been derived to supplement the PNS solutions and permit extrapolation of those results to higher angles of attack. The expression for C_A is based upon heat-transfer measurements on the windward side of the orbiter and Reynolds analogy relating the skin-friction coefficient to Stanton number. The details of this derivation are given in Ref. 13, but the final expression is

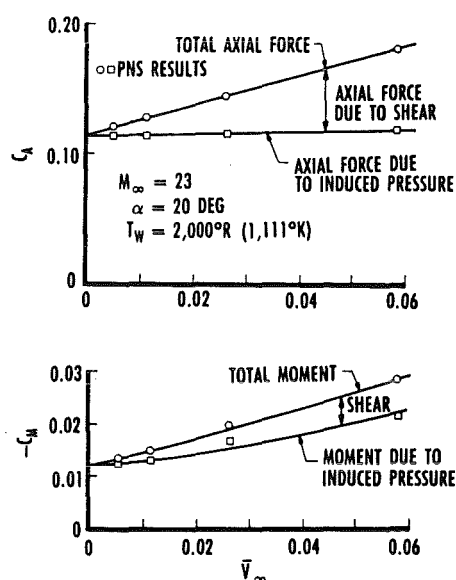


Figure 27. PNS computations of axial-force and pitching-moment coefficients.

$$C_A = 3.63 \bar{V}_\infty \sin \alpha (\cos \alpha)^{1.75} \quad (1)$$

where

$$\bar{V}_\infty = \frac{\sqrt{C_\infty} M_\infty}{\sqrt{Re_{\infty, L}}}$$

and

$$C_\infty = \frac{\mu_W T_\infty}{\mu_\infty T_W}$$

Eq. (1) is converted to an expression for viscous contribution to pitching moment by assuming that the viscous shear acts only over the windward surface and multiplying the force by an effective lever arm as shown in Fig. 28. The resulting expression is

$$C_M = -0.765 \bar{V}_\infty \sin (\cos \alpha)^{1.75} \quad (2)$$

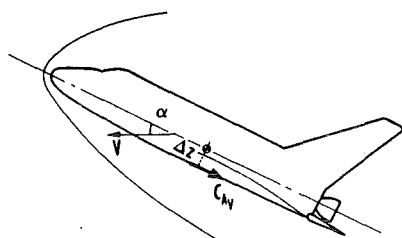


Figure 28. Empirical equation for viscous contribution to pitching moment.

ANALYTICAL APPROACH

* ASSUMPTION

- + VISCOUS DRAG AND VISCOUS MOMENT COMES FROM LOWER SURFACE ONLY.
- + VISCOUS MOMENT CAN BE EXPRESSED IN TERMS OF VISCOUS DRAG.

$$\begin{aligned} \Delta C_{My} &= C_{Ay} \cdot \frac{\Delta z}{\bar{c}} \\ &= -0.765 \bar{V}_\infty \sin \alpha (\cos \alpha)^{1.75} \end{aligned}$$

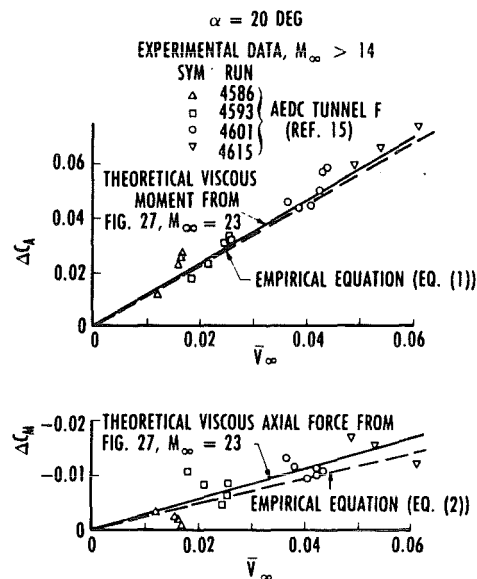


Figure 29. Comparison of theoretical, empirical, and experimental viscous drag and moment results.

Figure 29 shows a comparison of the viscous contribution to C_A and C_M as obtained from Eqs. (1) and (2) with corresponding PNS solutions and experimental data¹⁵ from AEDC Tunnel F at 20-deg angle of attack. The various experimental points shown for a given Tunnel F run are data taken at different times during the run where \bar{V}_∞ is changing because of decreasing stagnation pressure and varying stagnation temperature. Inviscid values of 0.0520 (C_A) and 0.001 (C_M) were subtracted from the tabulated experimental data in Ref. 15 to obtain ΔC_A and ΔC_M . The empirical equations gave a very good representation of the viscous influence predicted by the PNS solution and displayed by the experimental data at this angle of attack.

AERODYNAMIC MODEL

In order to make comparisons with flight results, aerodynamic coefficients for the orbiter at flight conditions were obtained by applying corrections described in the previous sections to the Mach 8 wind tunnel data. This procedure is illustrated in Fig. 30. For the comparisons with flight data made in this section, the contributions of the control surface deflections were assumed to be as predicted before flight and given in the Aerodynamic Design Data Book (ADDB).¹⁶

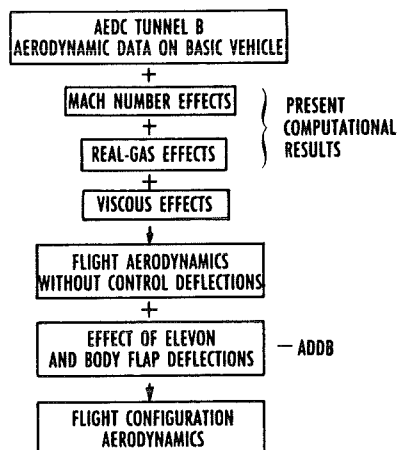


Figure 30. Methodology for extrapolation of aerodynamic data to flight conditions.

An example of the buildup of flight C_M is given in Fig. 31 for a high-altitude point on the flight trajectory. This figure shows the Mach 8 Tunnel B

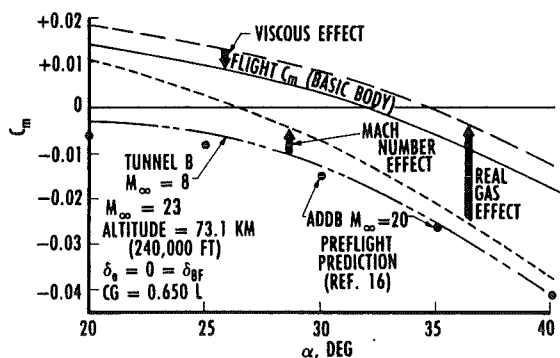


Figure 31. Build-up flight C_M using methodology.

data and the Mach number, real-gas, and viscous effects derived from CFD computations to arrive at the basic body C_M for the flight conditions. Also shown in this figure are the pre-flight predictions¹⁶ of C_M for similar conditions. Note that the basic body values of C_M from the aerodynamic model are 0.02 or more greater than the pre-flight predictions.

Figure 32 shows basic pitching-moment coefficient as obtained from the model as a function of Mach number and altitude for angles of attack of 30 and 40 deg. The trajectory of STS-3 is also plotted on this figure.

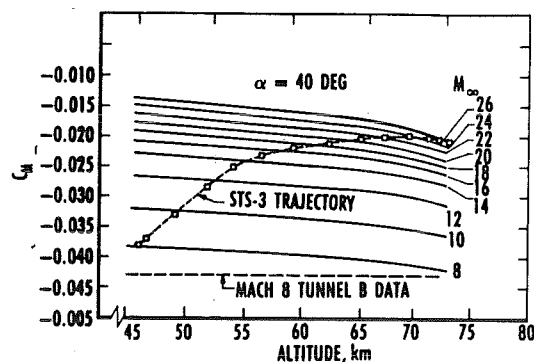
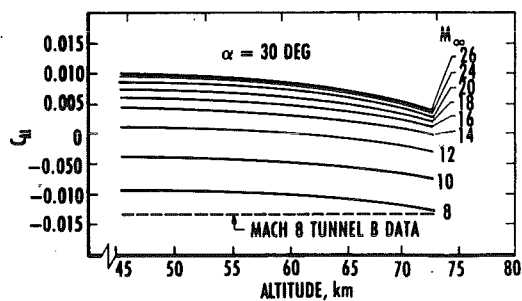


Figure 32. Basic body pitching-moment coefficient from methodology.

Comparison of the aerodynamic model with flight inferred values of C_M for STS-3 and STS-4 is displayed in Figs. 33 and 34. The C_M values plotted in these figures contain contributions from the control surface deflections as well as the basic body.

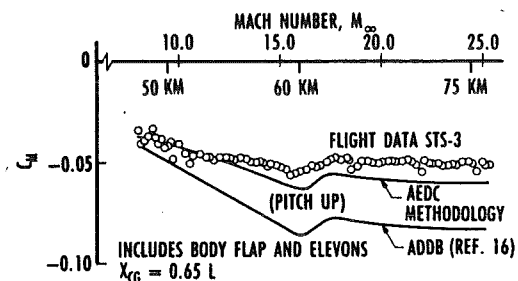


Figure 33. Comparison of aerodynamic predictions with flight data for STS-3.

Also shown in these figures are values from the Aerodynamic Design Data Book. The corrections for Mach number, real-gas, and viscous effects have accounted for approximately 75 percent of the discrepancy in pitching moment.

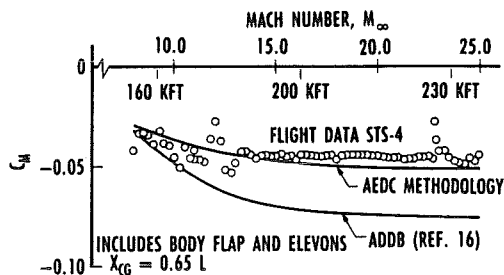


Figure 34. Comparison of aerodynamic predictions with flight data for STS-4.

BODY FLAP INVESTIGATION

An investigation of the body flap effectiveness was carried out in a manner similar to that performed on the basic vehicle itself. The body flap was modeled as a two-dimensional compression corner as shown in Fig. 35, and computations of the flow field were made using time-marching inviscid and viscous CFD codes. Initial profiles near the body flap hinge line, needed to start these computations, were obtained from Stein or PNS solutions for the model computational geometry. Figure 36, for example, shows velocity profiles from the PNS code at the body-flap hinge line for $\alpha = 20$ deg and several simulated altitudes at Mach 23. The projection of the body flap into the flow stream for 5- and 8 deg deflections are also given in this figure.

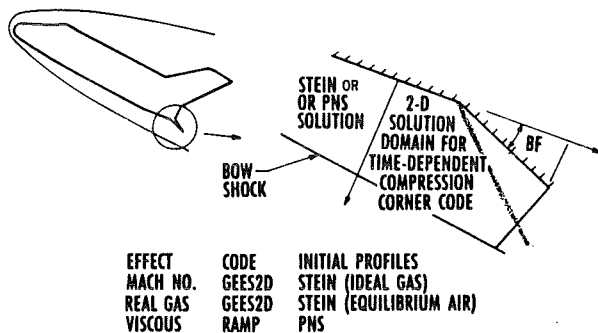


Figure 35. Computational domain and codes for control surface study.

Inviscid Computations

An investigation of Mach number and real-gas effects on the body flap effectiveness was carried out using a two-dimensional, time-marching Euler solver, GEES2D. The code employs an explicit MacCormack predictor-corrector algorithm to solve the two-dimensional Euler equations cast in conservation law form to permit shock capturing. An elliptic grid

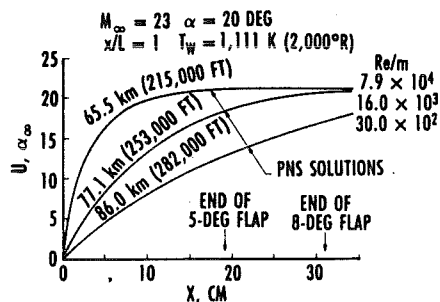


Figure 36. Velocity profiles at the body flap hinge line.

generator is used to map the solution domain between the body surface and the bow shock into a rectangular computational domain. Profiles on the windward centerline of the orbiter at the body flap hinge line obtained from STEIN solutions were used as initial conditions for the body flap computations. Rather than attempt to capture the bow shock, the outer boundary for the computation was taken to be just inside the shock where conditions were assumed to be constant. Experimentation showed the computed surface pressures to be insensitive to outer boundary conditions.

At the time of this study, GEES2D was restricted to perfect-gas computations; thus, the real-gas effects were simulated using a constant effective approximation. The value of γ used in the flap region was the average isentropic exponent calculated from the STEIN equilibrium air solution at the starting plane. Figures 37 and 38 show computed pressure contours in the flap region for ideal and simulated real-gas calculations, respectively. The change in embedded shock angle and structure between the two cases is apparent.

The influence of Mach number and effective gamma on the body flap contributions to vehicle pitching moment is shown in Fig. 39. The upper portion of this figure for $M_\infty = 8.0$ shows excellent agreement with values from the ADDB. Computational results for $M = 23$ are given in the lower part of the figure for $\gamma = 1.4$, and show a small Mach number effect, but a more substantial real-gas effect increasing the body flap effectiveness. This increase is primarily due to higher Mach numbers approaching the results with ADDB body flap for equilibrium air solution. An increase in body flap effectiveness is in the wrong direction to explain the differences shown in Figs. 33 and 34.

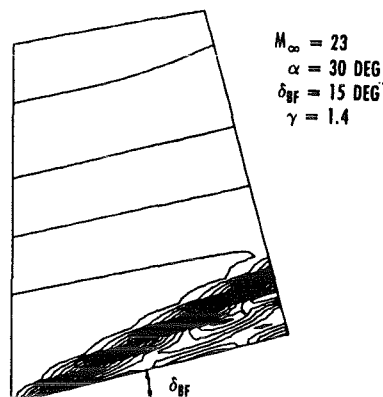


Figure 37. Inviscid pressure field near the body flap, $\gamma = 1.4$.

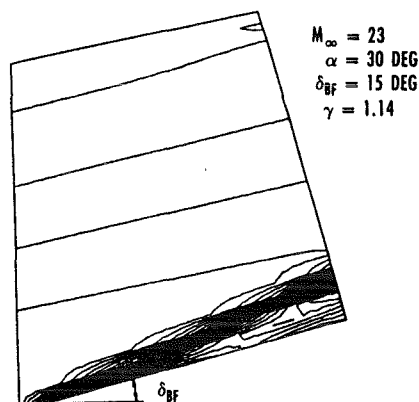


Figure 38. Inviscid pressure field near the body flap, $\gamma = 1.4$.

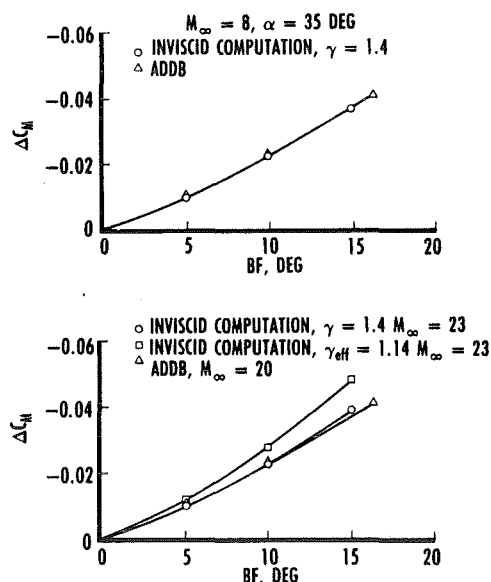


Figure 39. Comparison of inviscid computational results with ADDB body flap effectiveness.

Viscous Computations

The influence of viscosity on the body flap effectiveness is illustrated in Fig. 40 for an angle of attack of 20 deg. The upper part of the figure corresponding to wind tunnel conditions shows little change attributable to viscous effects. The lower graph, corresponding to conditions at 240 kft, shows a substantial loss of effectiveness. Unfortunately, viscous solutions for the basic body at higher angles of attack are not available to provide a starting data plane for the flap computations. However, an estimate of viscous effects on the body flap at high angles of attack was obtained by using inviscid basic body computations and scaling the boundary-layer thickness, from flat plate relations, using the local Mach number and Reynolds number at the body flap hinge line. This technique provided an approximate starting plane for the body flap computations for $\alpha > 20$ deg.

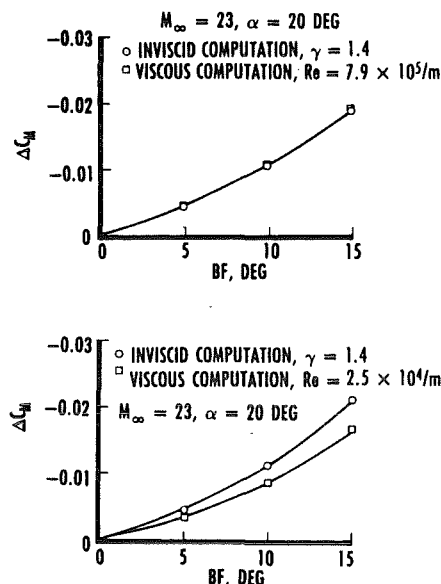


Figure 40. Viscous effect on body flap pitching moment.

The net result of the computed increase in effectiveness due to real gas and decrease due to viscous effects is shown in Fig. 41 for an angle of attack of 35 deg. The CFD computations suggest that the increase in effectiveness due to real-gas effects cancels the loss due to viscous effects.

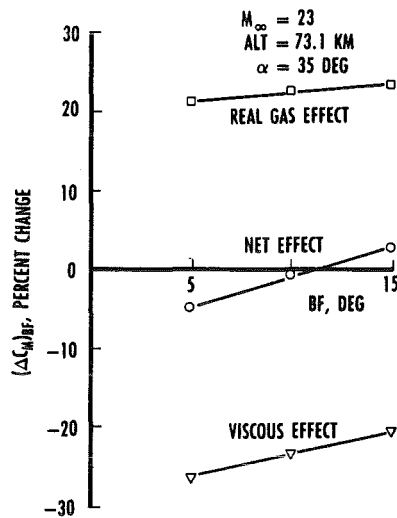


Figure 41. Real-gas and viscous influence on body flap effectiveness.

Flexibility Correction

There is a definite indication of a loss of body flap effectiveness in the orbiter flight data. This is shown in Fig. 42 where the residual in pitching moment for the first ten flights, computed using ADDB aerodynamics, is plotted versus body flap deflection. The trend exhibited by the data indicates that the body flap is less effective than predicted by the ADDB.

During the course of this investigation, some static deflection data on the body flap came to light implying a flexibility correction between the indicated and actual flap deflection at flight conditions. These tests were conducted by Rockwell International before STS-1, but were not included in the ADDB. Figure 43 shows the degree of error in the indicated flap deflection. This correction was included in the aerodynamic model.

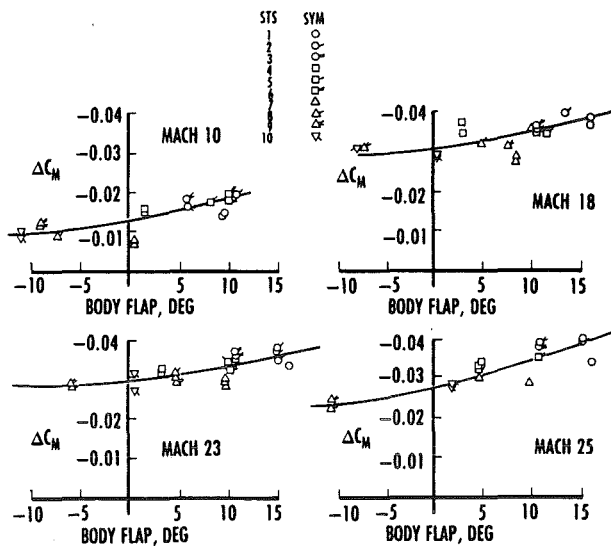


Figure 42. Moment residual about CG based on ADDB aerodynamics.

COMPARISON WITH FLIGHT DATA

The ultimate test for an aerodynamic model, of course, is how well it compares with flight data. The aerodynamic methodology presented in this paper has been compared with data from the first ten shuttle flights. The results of this comparison in terms of moment residual at four different Mach numbers are presented in Fig. 44 versus body flap deflection angle. A similar comparison based on ADDB aerodynamics is shown in Fig. 42, and the improvement is obvious. The moment residuals, ΔC_M , plotted in Figs. 42 and 44 were determined by summing moment contributions about the vehicle CG. If the aerodynamic coefficients, the free-stream dynamic pressure, and the vehicle CG were known precisely, this sum should be exactly zero for a trimmed flight condition. A negative ΔC_M indicates a positive contribution to C_M not accounted for in the aerodynamic model.

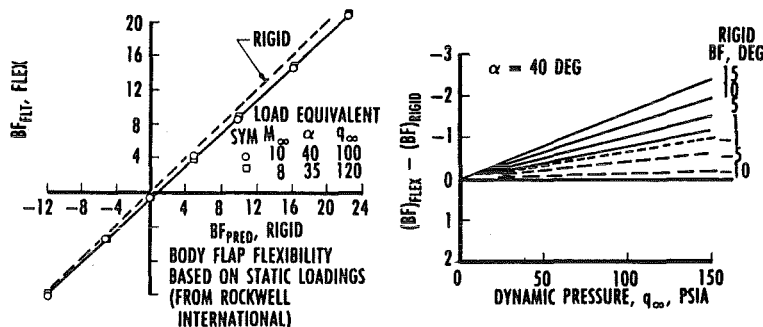


Figure 43. Body flap flexibility.

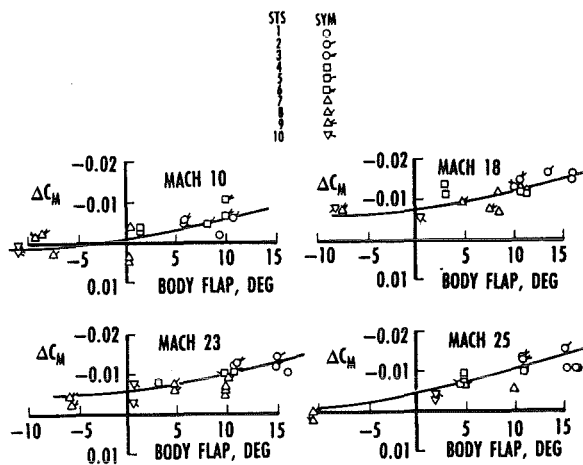


Figure 44. Moment residual about CG based on aerodynamic model.

Figure 45 shows a direct comparison of body flap deflection as computed with the current aerodynamic model with the flight data from STS-1. This represents about the poorest agreement between the model and any of the first ten flights. Also shown in Fig. 45 is the preflight prediction based on the ADDB.

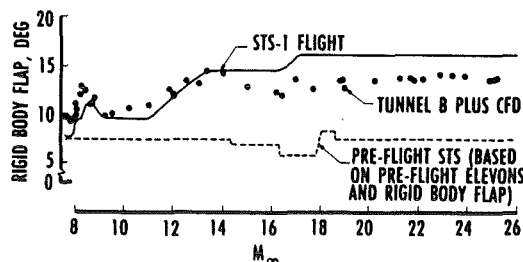


Figure 45. Comparison of predicted body flap deflection with flight data.

Two difficulties in the analysis of the shuttle flight data should be mentioned. A lack of precise knowledge of the atmospheric density, particularly at high altitude, introduces errors in reducing the aerodynamic forces to coefficient form. Also, the center of gravity of the vehicle is subject to an uncertainty of ± 2.0 cm. These uncertainties contribute to the data scatter in Figs. 42 and 44 and add challenge to the analysis of flight data.

Despite the much better agreement, there is still room for improvement between the aerodynamic model and the flight data. In particular, the trend in Fig. 44 suggest, that further loss in body flap effectiveness is present than just the small flexibility correction contained in the current model. This

difference is not surprising in view of the many assumptions made in the control surface analysis. There also appears to be an additional nose-up basic body pitching moment unaccounted for in the present model. Among the possibilities for this discrepancy are geometrical differences between the orbiter and the computational model, nonequilibrium effects, viscous cross-flow effects, and coupled real-gas viscous effects.

SUMMARY AND CONCLUSIONS

Inviscid and viscous CFD codes have been applied to a modified space shuttle orbiter geometry to investigate differences between preflight aerodynamic predictions and aerodynamic data from hypersonic reentry flight. The computer codes used have been tested by comparing surface pressure, heat transfer, and force coefficients with experimental data from AEDC wind tunnels. Flow-field solutions were obtained for flight conditions to assess Mach number, real-gas, and viscous effects on the reentry aerodynamics of the orbiter. Based on the CFD studies and a semi-empirical analysis of viscous forces, an aerodynamic model was developed to extrapolate wind tunnel data to flight conditions.

Comparison of the aerodynamic model with flight data shows a significant improvement over preflight predictions. Based on this study, the following conclusions are drawn:

1. Differences between preflight predictions and flight data for hypersonic pitching moment are primarily due to Mach number and real-gas effects.
2. Viscous effects have a stabilizing influence on orbiter aerodynamics.
3. Real-gas and viscous effects tend to produce opposite results on the control surfaces and cancel out.

REFERENCES

1. Romere, P. O. and Whitnah, A. M. "Space Shuttle Entry Longitudinal Aerodynamic Comparisons of Flights 1-4 with Preflight Predictions." *Shuttle Performance-Lessons Learned*, NASA CP 2283, March 1983.

2. Jordan, J. L. "NASE/RI OA 208 and 258 Verification Static-Stability and Control-Effectiveness Tests of the Space Shuttle Orbiter Vehicle at Mach Numbers from 2 to 8." AEDC-TSR-78-V6, June 1978.
3. Martindale, W. R. and Carter, L. D. "Flow-Field Measurements in the Windward Surface Shock Layer of Space Shuttle Orbiter Configuration at Mach Number 8." AEDC-TR-75-5 (AD-A012-875), July 1975.
4. Vachris, A. F. and Yeager, L. S. "Quick Geometry - A Rapid Response Method for Mathematically Modeling Configuration Geometry." NASA SP 390, 1975.
5. Hall, D. W. "Inviscid Aerodynamic Predictions for Ballistic Reentry Vehicles with Ablated Nostips." Science Applications, Inc. Report SAI-79-506-VF, February 1979.
6. Marconi, F., Dalas, M., and Yeager, L. Development of a Computer Code for Calculating the Steady Super/Hypersonic Inviscid Flow around Real Configurations." NASA-CR-2675, April 1975.
7. Maus, J. R., Griffith, B. J., Szema, K. Y., and Best, J. T. "Hypersonic Mach Number and Real Gas Effects on Space Shuttle Orbiter Aerodynamics." AIAA Paper 83-0343, January 1983.
8. Pulliam, T. H. and Steger, J. L. "On Implicit Finite-Difference Simulations of Three Dimensional Flow." AIAA Paper 78-10, January 1978.
9. Kutler, P., Perdelty, J. A., and Pulliam, T. H. "Hypersonic Flow Over Three-Dimensional Ablated Nostips using an Unsteady Implicit Numerical Procedure." AIAA Paper 80-0130, January 1980.
10. Schiff, L. B. and Steger, J. L. "Numerical Simulation of Hypersonic Viscous Flows Over Arbitrary Geometries at High Angles-of-Attack." AIAA Paper 81-0050, Jan. 1981.
11. Chausee, D. S., Patterson, J. L. Kutler, P., Pulliam, T. H., and Steger, J. L. "A Numerical Simulation of Hypersonic Viscous Flows Over Arbitrary Geometries at High Angles-of-Attack." AIAA Paper 81-0050, January 1981.
12. Shanks, S. P., Srivavasan, G. R., and Nicolet, W. E. "AFWAL Parabolized Navier-Stokes Code: Formulation and User's Manual." AFWAL-TR-82-3034, June 1982.
13. Szema, K. Y., Griffith, B. J., Maus, J. R., and Best, J. T. "Laminar Viscous Flow-Field Predictions Of Shuttle-Like Vehicle Aerodynamics." AIAA Paper 83-0211, Jan. 1983.
14. Griffith, B. J. Maus, J. R., and Best, J. T. "Explanation of the Hypersonic Longitudinal Stability Problem — Lessons Learned." NASA Langley Conference on Shuttle Performance — Lessons Learned. March 8-10, 1983.
15. Data Management Services, Chrysler Corporation. "Results of an Investigation of Hypersonic Viscous Interaction Effects on an 0.01-Scale Shuttle Orbiter 51-0 Model in the AEDC-VKF Hypersonic Wind Tunnel." Report DMS-DR-2152, January 1976.
16. Russell, W. R. ed. "Aerodynamic Design Data Book, Vol. 1M, Orbiter Vehicle." Rochwill International Report SD72-SH-006, October 1978.